Dentate gyrus development requires a cortical hem-derived astrocytic scaffold.

Alessia Caramello[1], Christophe Galichet[1], Karine Rizzoti[1*] and Robin Lovell-Badge[1*].

1 Laboratory of Stem Cell Biology and Developmental Genetics, The Francis Crick Institute, 1 Midland Road, London NW1 1AT, UK.

* authors for correspondence karine.rizzoti@crick.ac.uk and robin.lovell-badge@crick.ac.uk.

ABSTRACT:

Astrocytes are necessary for neuronal functionality in the adult brain; but may also support embryonic development of its cytoarchitecture. They are generated after neurons from embryonic radial glial cells, following the gliogenic switch. Regulation of the switch, operated by several transcription factors, is fundamental for allowing coordinated interactions between neurons and glia. We deleted one such factor, *Sox9,* early during mouse brain development and observed perturbed astrogenesis and a significantly compromised dentate gyrus (DG). We dissected the origin of the defect, targeting *Sox9* deletion to either the DG neuronal progenitor domain or the adjacent cortical hem (CH), and identified previously uncharacterized ALDH1L1+ astrocytic progenitors in the CH, which form a fimbrial-specific glial scaffold necessary for neuronal progenitor migration towards the developing DG. Our results highlight the crucial role of SOX9 for astroglial potential and illustrate how formation of a local network, amidst cells originating from adjacent domains, underlays brain morphogenesis.

INTRODUCTION:

Neuroepithelial cells (NECs) are at the origin of all neurons, glia and stem cells found in the central nervous system (CNS)[1]. During early CNS development, NEC potential is initially restricted to a neuronal fate. But, at around E10.5 in the mouse, NECs undergo an irreversible switch, becoming radial glial cells (RGCs), which enable them to later generate astrocyte and oligodendrocyte progenitors[2]. Induction of gliogenic potential in RGCs is controlled via a feedback mechanism originating from newly differentiated neurons, which allows a spatio-temporal control of both the emergence and abundance of each cell type generated[3-5]. Consequently, the timely appearance of neuronal and supporting cell types favors local establishment of fundamental neuron-glia interactions, necessary for achieving correct CNS cytoarchitecture and functionality[6-8]. Amongst other roles, these interactions are crucial to support the migration of differentiating neurons from the ventricular zone, from which they emerge, to their final destination in the brain parenchyma[9]. For example, in the developing cortex, the basal process of each RGC supports the radial migration of the intermediate neuronal progenitors it gives rise to[10]. In the adult brain, astrocytes form a tubular structure around neuronal progenitors guiding them from the subventricular zone to the olfactory bulb[11,12]. However, because astrocytic commitment has been difficult to monitor in the embryo, since until recently specific markers were lacking to distinguish these from RGCs[13,14], a potential migratory supporting role of this lineage in the embryo has not been formally established[15].

The dentate gyrus (DG) of the hippocampus, is a packed V-shaped layer of granule neurons involved in spatial memory formation and pattern separation[16], which hosts a niche of RG-like cells supporting adult neurogenesis[17]. During embryonic development, DG granule neuron progenitors originate from the dentate neuroepithelium (DNE) or primary (1ry) matrix of the archicortex. From E14.5 in the mouse, pioneer intermediate progenitors (IPs), followed by neural stem cells (NSCs) delaminate to migrate extensively within the parenchyma, along the Dentate Migratory Stream (DMS) or 2ry matrix[18]. From E16.5, this mixed cell population, which also comprises post-mitotic neurons at this stage, ultimately reaches the brain midline forming the 3ry matrix, where they distribute in the upper then lower blades of the DG, and differentiate into PROX1+ granule neurons[19]. This process continues until after birth, when 1ry and 2ry matrices eventually disappear, and formation of new granule neurons will exclusively rely on local adult neurogenesis[20]. The cortical hem (CH),

which is adjacent to the DNE and subsequently develops into the underlying fimbria, is a fundamental hippocampal organizer[21]. It gives rise to Cajal-Retzius (CR) cells, which regulate DG progenitor migration via secretion of Reelin and SDF1[22-24]. Progenitor migration occurs along the DMS on the track of RGC processes, which later develop into a GFAP+ glial scaffold, which stretches from both the DNE and fimbrial epithelium towards and around the forming DG[25]. Although definitive proof is lacking, the shape and directionality of GFAP+ filaments within the scaffold suggest a supportive role for progenitor migration, both along the 2ry matrix and within the 3ry matrix[22,23,26-31]. Furthermore, because GFAP is expressed by both RGCs and astrocytes, the cellular nature of the glial scaffold is unclear. Deletion of the transcription factors NF1A/B, which regulate astrocyte gene expression[32], partly affects formation of the scaffold, suggesting an astrocytic contribution[26,27,33]. Moreover, its formation is ambiguous, and it has been suggested to have a dual origin with a proximal fimbrial part deriving from the fimbrial glioepithelium, and a distal supragranular domain originating from DNE progenitors[23,26,31]. However, clear evidence of both cellular identity and regional origin are still lacking.

SOX9, an SRY-related high mobility group (HMG) box (SOX) transcription factor, starts to be expressed in NECs around E9.5, just before their transition to RGCs and neuro-to-glia switch. We and others showed that SOX9 is required for this process, both within the embryonic brain[34,35] and spinal cord[32,36], because generation of astrocytes and oligodendrocytes is affected by its deletion. More precisely, during spinal cord development, SOX9 regulates astrocytic gene expression via induction and subsequent interaction with NF1A[32]. In the absence of SOX9, NF1A expression is delayed and its transcriptional activity decreased[32], however this recovers subsequently, possibly because of compensatory pathways. The role of SOX9 during early CNS development has been analyzed in particular by conditional deletion using *Nestin-Cre*[37], but this only becomes active from E11.5, after the onset of SOX9 expression[34]. Consequently, the relatively mild effect of *Sox9* loss on astrogenesis in *Sox9$^{fl/fl}$;Nestin-Cre* mutants[32,36] might also be explained by its early, albeit temporary expression.

To better understand the role of SOX9 in CNS development, including at early stages, we performed conditional deletion using *Sox1$^{Cre/+}$*, which is active from E8.5 almost exclusively in the neural tube[38,39], and compared these with *Sox9$^{fl/fl}$;Nestin-Cre* mutants. In contrast with the latter model, *Sox9$^{fl/fl}$;Sox1$^{Cre/+}$* mutant mice survived,

allowing post-natal analysis. Reduced DG size was the most prominent defect in *Sox9*$^{fl/fl}$*;Sox1*$^{Cre/+}$ mutant brains and this was already visible in newborns, suggesting an earlier developmental defect. While the emergence and differentiation of granule neuron progenitors were not affected in either *Sox9* mutant embryos, we observed that their migration within the developing DG was compromised. We then showed that regional emergence of glial progenitors, and consequently formation of the glial scaffold supporting granule neuron progenitor migration was impaired in *Sox9*$^{fl/fl}$*;Sox1*$^{Cre/+}$ mutants. Furthermore, we demonstrate that these glial progenitors mostly form the fimbrial part of the glial scaffold and originate from the adjacent cortical hem (CH) where *Nestin-Cre* is only partially active, explaining the milder DG phenotype of *Sox9*$^{fl/fl}$*;Nestin-Cre* mutants. Moreover, expression of ALDH1L1 in these progenitors strongly suggests that the fimbrial scaffold is astrocytic. Exclusive deletion of *Sox9* in the CH, using *Wnt3a*^{iresCre} [21], further confirmed that SOX9 is required for astrocyte progenitor emergence and hence fimbrial glial scaffold formation, allowing neuron progenitor migration. Ultimately, our results highlight the crucial role of the timely emergence of glial progenitors for the establishment of a local supporting cellular network underlying neuronal migration and DG morphogenesis, and that, through its role in acquisition of astroglial potential, SOX9 is critical for this.

RESULTS:

Adult DG morphology is sensitive to precise patterns of *Sox9* deletion in the archicortex

To further characterize the role of SOX9 during CNS development, we first performed an early CNS specific conditional deletion of the gene by crossing *Sox9*$^{fl/fl}$ [40] with *Sox1*^{Cre}, which is active from E8.5[38] prior to the onset of SOX9 expression[34]. The birth, growth and survival of *Sox9*$^{fl/fl}$*;Sox1*$^{Cre/+}$ mice were not overtly affected. However, histological analyses of adult brains revealed that the DG was significantly reduced in size compared to controls (Fig. 1.Ai,ii;B). This was already evident at P2 (Fig. 1.Aiv-v), indicating that this phenotype might arise earlier, due to the absence of SOX9 during DG development.

Sox9$^{fl/fl}$*;Nestin-Cre* mutants[34] were generated in parallel, to examine morphogenesis of the DG in this model where *Sox9* is deleted 48 hours later, from E11.5, as it starts to be expressed in the developing CNS. In contrast with *Sox9*$^{fl/fl}$*;Sox1*$^{Cre/+}$ mutants,

most *Sox9*$^{fl/fl}$*;Nestin-Cre* animals die at birth[34]. Therefore, activity of *Nestin-Cre* outside the CNS[41], in tissues where SOX9 is required, such as pancreatic islets[42], heart[43] and/or kidneys[44], probably explains mortality of these mutants. We were, however, able to analyse two *Sox9*$^{fl/fl}$*;Nestin-Cre* animals that survived until around 3 months of age, and where loss of SOX9 was confirmed (Fig. S.1). In contrast with *Sox1*$^{Cre/+}$ mutants, the size of the DG in these two *Sox9*$^{fl/fl}$*;Nestin-Cre* animals was unaffected (Fig. 1.Aiii,B).

The difference in timing and/or pattern of *Sox9* deletion may underlie the variation in DG defects in the two mutant strains. To test this hypothesis, we analysed the activity of the two Cre drivers by lineage tracing using an *R26*^{ReYFP} allele and examined SOX9 expression in both mutant strains. At E11.5, eYFP reporter expression was observed throughout the forebrain in *Sox9*$^{fl/fl}$*;Sox1*$^{Cre/+}$*;R26R*$^{eYFP/+}$ embryos (Fig. 1.Diii) where, compared to controls, SOX9/*Sox9* expression was absent (Fig. 1.Dii,iv and Fig. S.2). However, in *Sox9*$^{fl/fl}$*;Sox1*$^{Cre/+}$ mutant archicortices, we detected some rare *Sox9* positive cells by *in situ* hybridization (Fig. S.2, see also Fig. 4), demonstrating that recombination of the *Sox9* allele is not quite ubiquitous. In contrast, *Nestin-Cre* is only active ventrally at E11.5, gradually progressing dorsally later in gestation (Fig. 1.Dv-x, Fig. S.2). This implies that in *Sox9*$^{fl/fl}$*;Nestin-Cre* mutants, SOX9 is transiently expressed in the DNE between E12.5 and E13.5 (Fig. 1.Eiii,vi). In addition, the adjacent CH (Fig. 1.F) presents a mosaic pattern of recombination in *Nestin-Cre* mutants, as previously shown[23]. Consequently, many SOX9 expressing cells can still be found at E16.5 in this region in *Sox9*$^{fl/fl}$*;Nestin-Cre* mutants (Fig. 1.Exii).

Altogether these results suggest that delayed recombination in the DNE and/or residual expression of SOX9 in the CH of *Sox9*$^{fl/fl}$*;Nestin-Cre* embryos underlie the difference in adult DG phenotype observed between *Sox9*$^{fl/fl}$;*Sox1*$^{Cre/+}$ and *Sox9*$^{fl/fl}$*;Nestin-Cre* mutants. Comparative analysis of DG development was then performed in these two models to characterize the origin of the defect observed in *Sox9*$^{fl/fl}$;*Sox1*$^{Cre/+}$ mutants.

Abnormal distribution of granule neurons and their progenitors in the developing DG of *Sox9* mutants.

DG neuronal progenitors and differentiating granule neurons were first examined by analyzing respectively the expression of the transcription factors TBR2[45] and PROX1[46] at different stages of embryonic (E14.5, E16.5, E18.5) and post-natal (P2)

DG development (Fig. 2.A,C) in *Sox9*$^{fl/fl}$*;Sox1*$^{Cre/+}$ and *Sox9*$^{fl/fl}$*;Nestin-Cre* mutants and controls. Both cell types were found in the same numbers at all embryonic stages in both *Sox9* mutant strains compared to controls (Fig. 2.B,D). In contrast, at P2 there appears to be a reduction in the number of both TBR2+ and PROX1+ cells in the mutants compared to controls (Fig. 2.B,D); although this is statistically significant only for the former, with 27% fewer cells (Fig. 2.B). Analysis of cleaved Caspase-3 immunostaining showed comparable patterns of cell apoptosis between mutants and controls, suggesting *Sox9* deletion does not affect progenitor survival at this stage (Fig. S.3). EdU labelling, revealed no difference between controls and mutants in emergence, expansion and differentiation of granule neuron progenitors (Fig. S.4). Altogether, these data indicate that the total number, survival and emergence of granule neurons and their progenitors are normal in both *Sox9*$^{fl/fl}$;*Sox1*$^{Cre/+}$ and *Sox9*$^{fl/fl}$*;Nestin-Cre* mutant embryos. However postnatally, a decrease in numbers of both cell types, albeit only significant for TBR2 progenitors, becomes apparent, particularly in *Sox9*$^{fl/fl}$*;Sox1*$^{Cre/+}$ animals.

While the total number of progenitors and granule neurons was unaffected in *Sox9* mutant embryos compared to controls, we observe an abnormal distribution of these cells along the three matrices (1ry, 2ry and 3ry) (Fig.2.A,C,E). At E18.5, we counted more TBR2+ cells in the 2ry matrix in *Sox9*$^{fl/fl}$*;Nestin-Cre* mutants, apparently at the detriment of the 3ry matrix, where fewer cells were present in both *Nestin-Cre* and *Sox9*$^{fl/fl}$*;Sox1*$^{Cre/+}$ mutants compared to controls (Fig. 2.Ei). The misdistribution of TBR2+ cells become more evident post-natally, with fewer TBR2+ progenitors in the 3ry matrix of both mutant strains, but with more cells present in the 1ry matrix of *Sox9*$^{fl/fl}$*;Sox1*$^{Cre/+}$ embryos and in the 2ry matrix of *Sox9*$^{fl/fl}$*;Nestin-Cre* mutants, compared to controls (Fig. 2.Eii). We analyzed in parallel the distribution of TBR2+EdU+ progenitors at P2 and confirmed this was abnormal in *Sox9*$^{fl/fl}$*;Sox1*$^{Cre/+}$ mutants, while *Sox9*$^{fl/fl}$*;Nestin-Cre* mutants were less affected (Fig. S.4.D). Similarly, in both *Sox9* mutants at P2, we observed a reduction in PROX1+ differentiating granule neurons in the 3ry matrix and, in parallel, a tendency of increased number of these cells in 1ry and 2ry matrices, which however reached significance only in the 1ry matrix *Sox9*$^{fl/fl}$*;Sox1*$^{Cre/+}$ mutants (Fig. 2.Eiii).

Furthermore, the distribution of PROX1+ cells within the 3ry matrix also appears disrupted at E18.5 in both mutants, albeit less severely in *Sox9*$^{fl/fl}$*;Nestin-Cre* embryos (Fig. 2.Ciii-v). To assess this defect, we quantified the number of PROX1+ cells in

different bins ranging from the lower to the upper blade (Fig. 2.F). In controls, PROX1+ cells are equally distributed between the upper and lower blade. In contrast, in *Sox9*$^{fl/fl}$*;Sox1*$^{Cre/+}$ mutants, these cells accumulate in the lower blade of the developing DG at the detriment of the upper blade, indicating that distribution of granule neurons is compromised between DG upper and lower blades in absence of SOX9. A similar tendency is observed in *Nestin-Cre* mutants; however, this does not reach statistical significance (Fig. 2.F). Finally, we also noticed in both mutant strains an ectopic cluster comprising a mix of both TBR2 and PROX1 positive cells accumulating close to the ventricle (arrows in Fig. 2A.iv,v,vii,viii, Cvii,viii).

Altogether these analyses show that progenitors and granule neurons are abnormally distributed in the developing DG of *Sox9* mutants, with *Sox1*^{Cre} mutants being more severely affected, both along the primary-to-tertiary matrix axis (Fig. 2.E) as well as within the forming DG (3ry matrix; Fig. 2.F). These observations suggest a defect in cell migration. The presence of an ectopic cluster of cells close to the ventricle is in agreement with this hypothesis, and we thus decided to characterize this further.

Cell migration is impaired in the developing DG in absence of SOX9.

We first analyzed the cellular composition of the ectopic cluster at P2 (Fig. 3.A-E). It is located next to the SOX2+ DNE (Fig. 3.Aiv-vi), and contains some SOX2+ progenitors and TBR2+ intermediate progenitors (some of which are EdU+; Fig. 3.Aiv-xviii). Moreover, we observed ectopic expression of PROX1 next to the DNE (arrows in Fig. 3.C) indicating that some progenitors are locally differentiating in granule neurons at this stage. Their commitment towards a granular cell fate was already visible at E18.5, with cells in the ectopic cluster expressing NeuroD1, required for maturation of granule neurons[47] (arrows in Fig. 3.D). In conclusion, the ectopic cluster comprises cells at different stages of commitment toward the granule neuron fate.

In the initial analysis of TBR2+ cell distribution (Fig. 2.A.Eii, iii), those present in the ectopic cluster were included into the 2ry matrix numbers (ectopic cluster + migrating cells within the 2ry matrix). To quantify the size of the ectopic cluster, which is indicative of the potential migration defect, we calculated the percentage of TBR2+ cells clustering in the ectopic cluster relative to the total number of TBR2+ cells in the 2ry matrix. The size of the ectopic cluster represents a significant proportion of TBR2+ cells within the 2ry matrix, and was similar in both *Sox9*$^{fl/fl}$*;Sox1*$^{Cre/+}$ (34.1±2.3%) and *Sox9*$^{fl/fl}$*;Nestin-Cre* (28.4±3.1%) mutants at E18.5 (Fig. 3.Ei). While this proportion

remained similar in *Sox9*$^{fl/fl}$*;Sox1*$^{Cre/+}$ mutants at P2 (36.7±5.3%), it was significantly decreased in *Sox9*$^{fl/fl}$*;Nestin-Cre* animals (17.9±3.4%), in agreement with their milder phenotype (Fig. 3.Ei). A similar distribution was observed for newly generated progenitors at P2, with 40.13±6.79% of TBR2+EdU+ cells of the 2ry matrix clustering in the ectopic cluster in *Sox9*$^{fl/fl}$*;Sox1*$^{Cre/+}$mutants, while this proportion is more than halved in *Sox9*$^{fl/fl}$*;Nestin-Cre* counterparts (18.0±3.5%; Fig. 3.Eii).

The presence of the ectopic cluster could be explained either by precocious differentiation of neuronal progenitors next to the ventricle or by their impaired migration toward the developing DG. To further analyze this aspect, lineage tracing of progenitors was performed using *in utero* electroporation in wild-type and *Sox9*$^{fl/fl}$*;Sox1*$^{Cre/+}$ mutants. Progenitors facing the ventricle were electroporated at E15.5 with a plasmid expressing dsRed and the distribution of dsRed+ cells within the 3 matrices was analyzed 7 days later at P2 (Fig. 3.F,G). The total number of dsRed+ cells within the developing DG at P2 was significantly lower in *Sox9*$^{fl/fl}$*;Sox1*$^{Cre/+}$ mutants compared to controls (Fig. 3.H). We did not observe excess cell death in electroporated mutants compared either to the contralateral side, or to controls at this stage (Fig. S.5). However, electroporated mutant progenitors, whose survival may have been compromised by lack of SOX9, may have been lost earlier. In controls, 33.4±7.26% of dsRed+ cells were PROX1+. In mutants, an average of 16.4±15.11% of dsRed+ cells were PROX1+, and this was not significantly different from controls. However, this proportion was variable. This may be explained by variability in the domain targeted by the electroporation since our previous data (Fig. 2.D) showed that loss of SOX9 does not have an effect on granule neuron differentiation. We then analyzed the distribution of dsRed+ cells in each matrix. In P2 controls, the highest proportion of dsRed+ cells was observed in the 3ry matrix (51.27±14.20%), demonstrating that an important fraction of E15.5 electroporated progenitors had given rise to migrating granule neurons that successfully reached their destination in the developing DG (Fig. 3.G,J). In contrast, in *Sox9*$^{fl/fl}$*;Sox1*$^{Cre/+}$ mutants, the highest proportion of dsRed+ cells was found in the 2ry matrix (39.18±13.59%) and the fraction of cells remaining in the 1ry matrix was significantly higher than in controls (Fig. 3.G,J). This suggests that, in *Sox9* mutants, a proportion of electroporated progenitors remained trapped near the DNE. These results are thus in agreement with impaired neuronal progenitor migration in the developing DG of *Sox9* mutants. We then

investigated the origin of this phenotype by examining known molecular mechanisms regulating this process.

Delayed induction of GFAP+ glial scaffold and its progenitors in absence of SOX9

We initially examined the expression of chemokines (*Reln*, *Cxcl12*) and their receptors (*Vldlr*, *Cxcr4*) known to be involved in early stages of DG progenitor migration[30,48]. Quantitative PCR did not reveal any significant change in *Sox9* mutant E12.5 dissected archicortices compared to controls (Fig. S.6.A). These results are consistent with the absence of early migration defects in *Sox9* mutants. In fact, cell accumulation only becomes evident at later stages of DG development, from E18.5. Even at this stage, Reelin expression pattern and intensity appeared unchanged in both *Sox9* mutants compared to controls (Fig. S.6.B) suggesting that CR cells, secreting Reelin, are not affected by loss of *Sox9*.

In addition to CR cells, a GFAP expressing glial scaffold is involved in DG progenitor migration[26]. We thus examined expression of GFAP and observed a strongly positive scaffold in control samples from E18.5 connecting the DNE to the forming DG, through the fimbria (Fig. 4.Ai, B). In contrast, this is almost absent in *Sox9*$^{fl/fl}$*;Sox1*$^{Cre/+}$ (Fig. 4.Aii) but only partially affected in *Sox9*$^{fl/fl}$*;Nestin-Cre* embryos, where the supragranular glial bundle is missing, but the fimbrial glial bundle is still visible (inset Fig. 4.Aiii). GFAP expression and scaffold structure in both *Sox9* mutants partially recover by P2 (Fig. 4.Aiv-vi, quantified in C), suggesting that absence of SOX9 might only delay scaffold formation, and that either compensatory or independent mechanisms may allow recovery early post-natally. However, the impact on DG morphogenesis is permanent.

Because SOX9 directly regulates the expression of *Gfap* in the developing spinal cord[32], absence of GFAP expression in *Sox9* mutants may simply reflect downregulation of the gene, rather than absence of the scaffold. In addition, GFAP is also expressed in radial-glial progenitors which may be affected in *Sox9* mutants[34]. Therefore, to confirm the transient defect in glial scaffold formation, we examined the expression of ALDH1L1, an astrocyte specific marker[49]. At E18.5, ALDH1L1 expression pattern overlaps with that of GFAP, particularly within the fimbria where we see many GFAP+;ALDH1L1+ fibers (arrowheads in inset b in Fig. 4.Di). In contrast, we observe GFAP+ALDH1L1- fibers around the developing DG (arrowheads in inset

a in Fig. 4.Di). At E16.5, before upregulation of GFAP, the ALDH1L1 expression pattern is reminiscent of that at E18.5, being still confined to the fimbria (Fig. 4.Dii). Finally, ALDH1L1+ cells are found as early as E13.5 in the archicortex (Fig. 4.Diii) and also at this stage, they are specifically localized in the LEF1-negative;SOX2^{high} CH[50] (Fig. 4.E). Altogether, these results indicate ALDH1L1+ cells are confined to the CH/fimbria throughout development suggesting they might represent the astrocytic progenitors of the fimbrial glial bundle.

We then analyzed whether ALDH1L1+ cells were affected by absence of SOX9. Strikingly, there was a dramatic reduction in their number in *Sox9$^{fl/fl}$;Sox1$^{Cre/+}$* mutants compared to controls, both at E13.5 and E16.5 (Fig. 4.F,G). Accordingly, *Aldh1l1* expression was significantly reduced in dissected archicortices of *Sox9$^{fl/fl}$;Sox1$^{Cre/+}$* E12.5 embryos compared to controls (Fig. 4.H). This is again consistent with a requirement for SOX9 for the emergence of astrocytic ALDH1L1+ progenitors, and consequently formation of the GFAP+ glial scaffold.

In contrast with *Sox9$^{fl/fl}$;Sox1$^{Cre/+}$* mutants, ALDH1L1+ cell number was unaffected in in *Sox9$^{fl/fl}$;Nestin-Cre*. Because *Nestin-Cre*-mediated recombination occurs within the CH in a salt and pepper manner, SOX9 and ALDH1L1 expression patterns were analyzed in this region in *Sox9$^{fl/fl}$;Nestin-Cre* mutants. At E13.5, ALDH1L1+ cells were expressing SOX9 in the CH of *Sox9$^{fl/fl}$;Nestin-Cre* embryos (Fig. 4.Iii,vi), and this was still observed at E16.5 (Fig. 4.Iiv,viii). Interestingly, some rare SOX9+ cells were also present in the CH of E13.5 *Sox9$^{fl/fl}$;Sox1$^{Cre/+}$* mutants, and some were ALDH1L1+ (Fig. 4.Ii,v). These results suggest that in the CH of the mutants, ALDH1L1+ cells may only arise from SOX9+ progenitors escaping Cre recombination, which are present in higher numbers in *Sox9$^{fl/fl}$;Nestin-Cre* compared to *Sox9$^{fl/fl}$;Sox1$^{Cre/+}$* mutants. This further confirms SOX9 requirement for emergence of astrocytic progenitors. Moreover, the correlation between the extent of ALDH1L1+ cell loss and, consequently, of the fimbrial glial bundle deficiency with the severity of the progenitor migration defect in *Sox9$^{fl/fl}$;Sox1$^{Cre/+}$* versus *Sox9$^{fl/fl}$;Nestin-Cre* mutants, indicates a supporting migratory role for the scaffold.

Finally, in the developing spinal cord, the expression of the transcription factors NF1A/B are regulated by SOX9 and this is important for astrocytic differentiation[32]. We thus examined expression of NF1A and B in *Sox9$^{fl/fl}$;Sox1$^{Cre/+}$* E12.5 embryos. Both genes are expressed in the archicortex in control embryos. Loss of SOX9 does not affect either NF1A/B protein or transcript levels (Fig. S.7). We conclude that distinct

molecular mechanisms downstream of SOX9 must underlie astrocytic specification in different domains of the CNS.

CH-specific deletion of *Sox9* using *Wnt3a*$^{iresCre/+}$ impairs fimbrial glial bundle formation and compromises granule neuron progenitor migration.

Because both *Sox1*$^{Cre/+}$ and *Nestin-Cre* are also active in the DNE (Fig. 1.E), cell autonomous defects could contribute to defective granule neuron progenitor migration. To examine this possibility and to confirm the requirement for SOX9 in CH for the formation of the fimbrial glial bundle, CH-specific deletion of *Sox9* was performed using *Wnt3a*^{iresCre} [21]. Specificity of *Wnt3a*^{iresCre} CH activity was first confirmed by lineage tracing in conjunction with LEF1 staining at E12.5 (Fig. 5.A). While YFP staining from the *R26R*^{eYFP} reporter is mostly confined to the CH, some eYFP+ cells were observed in the LEF1+ DNE (arrowheads in Fig. 5.A). The *Wnt3a*^{iresCre} recombination pattern was therefore analyzed at P2: only 6.5% of PROX1+ granule neurons were YFP+ (arrowheads in Fig. 5.Bi-iii, quantified in Fig. D). Conversely, the fimbrial glial bundle was entirely YFP+, demonstrating its CH origin (arrowheads in Fig. 5.Biv-vi). We observed some GFAP+ filaments in the DNE as well, which were YFP-, suggesting they represent DNE-derived radial glial cells (arrows in Fig. 5.Biv-vi). In addition, the supragranular glial scaffold is made of both YFP+ and YFP- fibers suggesting a dual DNE and CH origin (respectively arrowheads and arrows in Fig. 5.Bvii-ix). Altogether these results also show that *Wnt3a*^{iresCre} is a suitable Cre driver for CH-specific deletion of *Sox9*.

Sox9$^{fl/fl}$*;Wnt3a*$^{iresCre/+}$ mutants were then generated. While we were able to harvest mutant embryos until E18.5, animals died shortly after birth, precluding any post-natal analyses. *Wnt3a* is widely expressed in embryonic mesoderm precursors[51] and deletion of *Sox9* in the embryonic heart, skeleton, pancreas and kidney is known to result in post-natal lethality[42,43,44]. In *Sox9*$^{fl/fl}$*;Wnt3a*$^{iresCre/+}$ mutant CNS, SOX9 is absent specifically in the CH at E13.5 (Fig. 5.Fi-iv). Importantly, we also observe a 50% reduction of ALDH1L1+ cells in this area at E13.5 in mutants compared to controls (Fig. 5.E,Fv,vi). At E18.5, the GFAP+ fimbrial glial bundle is exclusively compromised in *Sox9*$^{fl/fl}$*;Wnt3a*$^{iresCre/+}$ mutants (Fig. 5.Fviii), while the supragranular one is unaffected (Fig. 5.Fviii). These results are consistent with a role for SOX9 in the CH for specification of the ALDH1L1+ astrocytic progenitors giving rise to GFAP+ fimbrial glial bundle. The normal appearance of supragranular glial bundle is

consistent with the observation that it arises from both the CH and the DNE (Fig. 5.Bvii-ix).

We then analyzed granule neurons and their progenitors in *Sox9*$^{fl/fl}$*;Wnt3a*$^{iresCre/+}$ mutants. At E18.5, the total number of PROX1+ granule neurons and TBR2+ progenitors is unchanged in mutants compared to controls (Fig. 6.A,B and Fig. 6.D,E respectively), similarly to what we observed in *Sox9*$^{fl/fl}$*;Sox1*$^{Cre/+}$ mutants. Therefore, CH-specific deletion of *Sox9* does not affect progenitor formation and differentiation. We then analyzed the distribution of the granule neurons. At E18.5, PROX1+ cell distribution in the upper and lower blades of the forming DG is unaffected in *Sox9*$^{fl/fl}$*;Wnt3a*$^{iresCre/+}$ mutants compared to controls (Fig. 6.A,C). This is consistent with the supragranular glial bundle not being significantly affected upon CH-specific deletion of *Sox9* (Fig. 5.Fviii), as it has been previously shown to be generated by cells deriving from the DNE[23,31]. In contrast, granule neuron distribution is severely compromised in *Sox9*$^{fl/fl}$*;Sox1*$^{Cre/+}$ and *Sox9*$^{fl/fl}$*;Nestin-Cre* mutants (Fig. S.8), in accord with a DNE contribution to the supragranular glial bundle, as in both mutants *Sox9* is deleted in this domain.

We then examined repartition of the TBR2+ progenitors in the three matrices at E18.5. We observe that more cells accumulate in the 2ry matrix of *Sox9*$^{fl/fl}$*;Wnt3a*$^{iresCre/+}$ mutants compared to controls (Fig. 6.F). This abnormal distribution is reminiscent of that seen in *Sox9*$^{fl/fl}$*;Sox1*$^{Cre/+}$ mutants (Fig. 2.D). Furthermore, progenitors in *Sox9*$^{fl/fl}$*;Wnt3a*$^{iresCre/+}$ mutants form a cluster close to the ventricle (the ectopic cluster; Fig. 6.Dii), with a size comparable to that seen in both *Sox9*$^{fl/fl}$*;Sox1*$^{Cre/+}$ and *Sox9*$^{fl/fl}$*;Nestin-Cre* mutants at the same stage (Fig. 6.G). The ectopic cluster comprises differentiating neurons, with some cells expressing NeuroD1 (arrow in Fig.6.H) as previously observed in *Sox9*$^{fl/fl}$*;Sox1*$^{Cre/+}$ and *Sox9*$^{fl/fl}$*;Nestin-Cre* mutants (Fig. 3.D). Defective localization is not due to cell autonomous defects, because cells accumulating in the ectopic cluster are reporter negative in E18.5 *Sox9*$^{fl/fl}$*;Wnt3a*$^{iresCre/+}$*;R26R*^{eYFP} mutants (Fig. 6.Lv-vii), indicating that their precursors were not deleted for *Sox9*. Altogether, these results strongly suggest that SOX9 is required in CH for astrocytic specification and subsequent fimbrial glial bundle formation. Furthermore, they demonstrate that defective localization of neuronal progenitors is a non-cell-autonomous defect, consistent with a lack of migratory support by the defective CH-derived fimbrial glial bundle (Fig. 6.Lviii).

DISCUSSION

Using conditional deletion approaches, we have dissected the role of SOX9 during DG development. Differential patterns of gene deletion in the archicortex had marked consequences on adult DG morphology, and we were consequently able to establish that SOX9 expression is required in the CH for proper DG morphogenesis. More precisely, our results highlight the crucial role of SOX9 for astroglial potential acquisition, enabling the timely emergence of glial progenitors in the CH, and subsequent formation of the fimbrial glial bundle. Moreover, we show that this astrocytic bundle is required to support granule neuron progenitor migration toward the future DG. Furthermore, despite partial recovery of the scaffold early post-natally in *Sox9* mutants, DG morphogenesis is permanently affected, demonstrating that while the astrocytic bundle is indispensable, its role is transient. In conclusion, our study unravels the cascade of events orchestrating the establishment of supportive astrocytic-neural interactions required for DG morphogenesis, highlighting its sensitivity to timing and dependence on SOX9.

Dual origin, function and nature of the DG glial scaffold

Lineage tracing experiments using *Wnt3a*^{iresCre} demonstrate here that the fimbrial part of the DG glial scaffold has a CH origin. Moreover, defects observed in its absence show that it supports neuronal progenitor and differentiating granule neuron migration from 1ry-to-3ry matrix. This had been suggested previously, but without direct evidence[23,26]. In agreement with a DNE origin for the distal part of the scaffold[23,31], the supragranular glial bundle, was mostly unlabelled in our *Wnt3a*^{iresCre} lineage tracing experiments. However, the presence of some labelled fibers suggests that there is a CH contribution for the distal part of the scaffold. Beside a different cellular composition, the supragranular scaffold has also been suggested to have a distinct function from the fimbrial one, where the former guides granule neuron migration within DG upper and lower blades[31]. In agreement, in *Sox9*$^{fl/fl}$*;Wnt3a*$^{iresCre/+}$ mutants, both the supragranular scaffold and the distribution of granule neurons in the 3ry matrix of the developing DG appear normal. We observe in contrast a transient impairment of this distal scaffold in both *Sox9*$^{fl/fl}$*;Sox1*$^{Cre/+}$ and, to a lesser extent, in *Sox9*$^{fl/fl}$*;Nestin-Cre* mutants, along with an altered upper/lower blade distribution of granule neurons. These results are in accord with a different role for this scaffold. Furthermore, they also support a predominant DNE origin since both *Sox1* and *Nestin-*

Cre drivers are active in this domain. In agreement with a contribution from the CH, the milder alteration in DG upper/lower blade granule neuron distribution in *Sox9*$^{fl/fl}$*;Nestin-Cre* may be explained by contribution of SOX9 positive, CH-derived glial cells, to the supragranular scaffold formation, because *Nestin-Cre* is only active in a proportion of the cells in this domain. In addition, because in *Sox9* mutants the ectopic cluster appears only from E18.5, the fimbrial glial scaffold may only become indispensable for migration at late stages of DG development. We hypothesize that this may be explained by the increasing distance between DNE and the forming DG, as development proceeds.

ALDH1L1 and GFAP co-expression in the fimbrial scaffold argue strongly for an astrocytic identity, demonstrating for the first time a migratory support role for this lineage in the mouse embryo. In the spinal cord, *Aldh1l1*-GFP is first detected at E12.5[52] and we observe a similar onset of expression of ALDH1L1 in the CH in presumptive astrocytic progenitors, which may represent the fimbrial glioepithelium[26]. This is in contrast with what is observed elsewhere in the developing forebrain where astrocytes are known to arise around E16.5[53], and suggests an earlier emergence in this region. Interestingly, CH derived CR cells are the first neurons generated in the brain[54]. Since the gliogenic switch is controlled by differentiating neurons[3], it is tempting to speculate that the initial emergence of CR cells may explain early gliogenic induction in the CH. Finally, in the supragranular scaffold, ALDH1L1 and GFAP are both present but they do not colocalise. This supports a mixed origin for this distal scaffold, and furthermore suggests a different cellular composition. In fact, exclusive expression of GFAP in some cells suggests that, in this domain, DNE-derived RGCs support neuronal distribution, in addition to some CH-derived astrocytic progenitors.

Other migration cues are necessary for granule neuron guidance. CH-derived CR cells play an important role through the release of chemokines, such as Reelin[30] and SDF1 (CXCL12)[55]. We did not observe any significant alteration in *Reelin* and *Cxcl12* expression indicating that CR cells are not affected by *Sox9* deletion. Therefore, our work highlights a crucial role for the fimbrial glial bundle for 1ry-to-3ry matrix progenitor migration from E18.5, while the supragranular scaffold facilitate 3ry matrix cell distribution. Further investigations are needed to characterize how the scaffolds support cell migration and distribution.

Role of SOX9 during DG morphogenesis.

Impairment of DNE progenitor migration in *Sox9*$^{fl/fl}$*;Wnt3a*$^{iresCre/+}$ mutants demonstrates that loss of SOX9 in these cells does not explain the migration defect. However, this does not rule out a role for SOX9 in DNE progenitors. Indeed, while we did not observe a significant alteration in progenitor emergence, differentiation and survival embryonically, there is a significant decrease in intermediate progenitor numbers early post-natally. This reduction coincides with formation of the ectopic cluster, where 35% of TBR2+ progenitors are unable to reach the developing DG in *Sox9*$^{fl/fl}$*;Sox1*$^{Cre/+}$ mutants. Their survival and expansion might be affected away from their destination, and account for the reduction in progenitor total numbers. While we did not detect a significant increase in apoptosis in the ectopic cluster at P2, these cells are absent in the adult brain, suggesting a post-natal loss. Alternatively, reduction of TBR2 cells could indicate that SOX9 is required for maintenance and/or expansion of migrating NSCs (Nelson et al, 2020), leading to post-natal reduction of a pool of newly formed TBR2 cells that was not detected by our analysis. We[34] and others[35,56] have indeed previously shown that SOX9 regulates progenitor formation and expansion. However, in other contexts, such a role was not observed[32,36,57,58]. This variability may depend on the cellular context, but timing of the deletion is also relevant. Compensation by other members of the SOXE family, in particular SOX8, has been shown to explain recovery of some defects due to *Sox9* loss[59]. In our context, it is likely that both compensatory mechanisms and timing contribute to the difference in the severity of the defects observed after *Sox9* loss in different models. Analysis of SOX9/SOX8 double mutants would clarify this possibility. Finally, SOX9 is also expressed in adult DG NSCs[60], and required for maintenance of SVZ NSCs[34]. Further analysis of the *Sox9*$^{fl/fl}$*;Sox1*$^{Cre/+}$ mutants is therefore required to investigate the potential contribution of impaired adult neurogenesis to the phenotype. Moreover, as discussed above, SOX9 is likely to be required in DNE progenitors for formation of the supragranular scaffold, most likely as an inducer of gliogenic or RGCs fate[34,36].

More clearly, the importance of SOX9 for the acquisition of gliogenic potential is demonstrated by the loss of the fimbrial scaffold in *Sox9*$^{fl/fl}$*;Wnt3a*$^{iresCre/+}$ mutants. In the astrocytic lineage, SOX9 expression is maintained at high levels[61] and it is required for astrocytic specification in the spinal cord[32] and anterior CNS[34,56,62]. In the spinal cord it has been shown to induce expression of NFIA, with which it then interacts to activate expression of astrocytic genes. In contrast, we show here that NF1A/B

expression is not affected in the developing forebrain following *Sox9* deletion. Therefore other factors and pathways must be involved for induction of *Nf1a* expression, which could include BRN2[63], WNT[64] and/or NOTCH[65]. Furthermore, as shown in the spinal cord[32], gliogenesis in CH is simply delayed in *Sox9*$^{fl/fl}$*;Sox1*$^{Cre/+}$ and *Sox9*$^{fl/fl}$*;Nestin-Cre* mutants. This could reflect a reduced transcriptional activity of NF1 factors without SOX9, as previously shown for NF1A (Kang et al, 2012). As discussed above, recovery could also be due to compensatory expression of SOX8. Further analyses are required to understand the mechanisms underlying recovery of the fimbrial scaffold.

It will be important to characterize the molecular mechanism utilized by the scaffold for supporting neuronal migration. Whether this support is based on release of chemoattractants and/or relies on cell-cell or cell-matrix interactions, is still unknown. For example, astrocytes from the fimbrial scaffold could form tubules around the migrating progenitors of the 2ry matrix, similarly to how this same cell type supports neuroblast migration along the rostral migratory stream of the adult brain[11,12]. This aspect of scaffold functionality could be addressed using *Aldh1l1-Cre*[52] to delete ligands potentially involved.

In addition, our CH lineage tracing analysis using *Wnt3a*^{iresCre} shows that around 6.5% of granule neurons are reporter positive, suggesting that a proportion of neuronal progenitors originates from the CH. This exciting possibility requires further confirmation with additional lineage tracing analyses. However, it suggests that this subpopulation may have different characteristics. Whether other cells forming the adult DG, such as adult NSCs, also originate from the CH, is unknown and requires further investigation.

In conclusion, SOX9 plays sequential roles during CNS development as cells progress from a NSC fate, in which the protein is required for induction and also maintenance, to acquisition of gliogenic potential. Experimental manipulation of its expression levels highlights aspects of its function, according to the cellular context and also timing, which is presumably explained by the pattern of expression of redundant SOXE members, and its different interactors. Here we reveal that DG development is particularly sensitive to early loss of *Sox9* due to the failure to generate an astrocytic scaffold that aids neuronal migration. Extensive cell migration[66] and progenitor pool expansion[67] might underlay the vulnerability of this region, illustrated by the lasting consequences of transiently impaired cell migration.

ACKNOWLEDGEMENTS

We are grateful for help and support from all past and present members of the Lovell-Badge's lab. We thank François Guillemot (the Francis Crick Institute) for helpful discussions. Distance.gui software for analysis of granule neurons distribution within the forming DG was written by Dr. Vivien Labat-gest and kindly donated by Prof. Federico Luzzati (Neuroscience Institute Cavalieri Ottolenghi – NICO). We also thank Dr. Lucas Baltussen for providing training for *in utero* electroporation and kind donation of pCAG-hyPBase and pPB-CAG-DsRed plasmids. Finally, we also thank Biological Services, Experimental Histopathology and Advanced light microscopy platforms at the Francis Crick Institute, for their excellent assistance and technical support and the Mutant Mouse Regional Resource Center U42OD010918 for providing aliquots of *Wnt3a*^{iresCre} cryo-preserved sperm.

This work was supported by the Medical Research Council, U.K. (U117512772, U117562207 and U117570590) and the Francis Crick Institute which receives its core funding from Cancer Research UK (FC001107), the UK Medical Research Council (FC001107), and the Wellcome Trust (FC001107).

BIBLIOGRAPHY:

1 Paridaen, J. T. M. L. & Huttner, W. B. Neurogenesis during development of the vertebrate central nervous system. *EMBO reports* **15**, 351 (2014).

2 Malatesta, P., Appolloni, I. & Calzolari, F. Radial glia and neural stem cells. *Cell Tissue Res* **331**, 165-178, doi:10.1007/s00441-007-0481-8 (2008).

3 Barnabé-Heider, F. *et al.* Evidence that Embryonic Neurons Regulate the Onset of Cortical Gliogenesis via Cardiotrophin-1. *Neuron* **48**, 253-265, doi:https://doi.org/10.1016/j.neuron.2005.08.037 (2005).

4 Sheikh, B. N. *et al.* Systematic Identification of Cell-Cell Communication Networks in the Developing Brain. *iScience* **21**, 273-287, doi:https://doi.org/10.1016/j.isci.2019.10.026 (2019).

5 Zarei-Kheirabadi, M., Vaccaro, A. R., Rahimi-Movaghar, V., Kiani, S. & Baharvand, H. An Overview of Extrinsic and Intrinsic Mechanisms Involved in Astrocyte Development in the Central Nervous System. *Stem Cells and Development* **29**, 266-280, doi:10.1089/scd.2019.0189 (2019).

6 Orduz, D. *et al.* Developmental cell death regulates lineage-related interneuron-oligodendroglia functional clusters and oligodendrocyte homeostasis. *Nature Communications* **10**, 4249, doi:10.1038/s41467-019-11904-4 (2019).

7 Lee, M. A., Sitko, A. A., Khalid, S., Shirasu-Hiza, M. & Mason, C. A. Spatiotemporal distribution of glia in and around the developing mouse optic tract. *The Journal of comparative neurology* **527**, 508-521, doi:10.1002/cne.24462 (2019).

8 Nichols, E. L., Green, L. A. & Smith, C. J. Ensheathing cells utilize dynamic tiling of neuronal somas in development and injury as early as neuronal differentiation. *Neural development* **13**, 19-19, doi:10.1186/s13064-018-0115-8 (2018).

9 Cooper, J. A. Mechanisms of cell migration in the nervous system. *The Journal of Cell Biology* **202**, 725, doi:10.1083/jcb.201305021 (2013).

10 Nadarajah, B. Radial glia and somal translocation of radial neurons in the developing cerebral cortex. *Glia* **43**, 33-36, doi:10.1002/glia.10245 (2003).

11 Lois, C., García-Verdugo, J.-M. & Alvarez-Buylla, A. Chain Migration of Neuronal Precursors. *Science* **271**, 978, doi:10.1126/science.271.5251.978 (1996).

12 Gengatharan, A., Bammann, R. R. & Saghatelyan, A. The Role of Astrocytes in the Generation, Migration, and Integration of New Neurons in the Adult Olfactory Bulb. *Frontiers in Neuroscience* **10**, 149 (2016).

13 Molofsky, A. V. *et al.* Expression Profiling of Aldh1l1-Precursors in the Developing Spinal Cord Reveals Glial Lineage-Specific Genes and Direct Sox9-Nfe2l1 Interactions. *Glia* **61**, 1518-1532, doi:10.1002/glia.22538 (2013).

14 Weng, Q. *et al.* Single-Cell Transcriptomics Uncovers Glial Progenitor Diversity and Cell Fate Determinants during Development and Gliomagenesis. *Cell Stem Cell*, doi:https://doi.org/10.1016/j.stem.2019.03.006 (2019).

15 Nguyen, H. *et al.* Glial scaffold required for cerebellar granule cell migration is dependent on dystroglycan function as a receptor for basement membrane proteins. *Acta Neuropathol Commun* **1**, 58-58, doi:10.1186/2051-5960-1-58 (2013).
16 Jessberger, S. *et al.* Dentate gyrus-specific knockdown of adult neurogenesis impairs spatial and object recognition memory in adult rats. *Learn Mem* **16**, 147-154, doi:10.1101/lm.1172609 (2009).
17 Ghosh, H. S. Adult Neurogenesis and the Promise of Adult Neural Stem Cells. *Journal of Experimental Neuroscience* **13**, 1179069519856876, doi:10.1177/1179069519856876 (2019).
18 Nelson, B. R. *et al.* Intermediate progenitors support migration of neural stem cells into dentate gyrus outer neurogenic niches. *eLife* **9**, e53777, doi:10.7554/eLife.53777 (2020).
19 Urbán, N. & Guillemot, F. Neurogenesis in the embryonic and adult brain: same regulators, different roles. *Frontiers in Cellular Neuroscience* **8**, doi:10.3389/fncel.2014.00396 (2014).
20 Nicola, Z., Fabel, K. & Kempermann, G. Development of the adult neurogenic niche in the hippocampus of mice. *Frontiers in Neuroanatomy* **9**, 53 (2015).
21 Yoshida, M., Assimacopoulos, S., Jones, K. R. & Grove, E. A. Massive loss of Cajal-Retzius cells does not disrupt neocortical layer order. *Development* **133**, 537, doi:10.1242/dev.02209 (2006).
22 Sibbe, M., Förster, E., Basak, O., Taylor, V. & Frotscher, M. Reelin and Notch1 Cooperate in the Development of the Dentate Gyrus. *The Journal of Neuroscience* **29**, 8578 (2009).
23 Li, G., Kataoka, H., Coughlin, S. R. & Pleasure, S. J. Identification of a transient subpial neurogenic zone in the developing dentate gyrus and its regulation by Cxcl12 and reelin signaling. *Development* **136**, 327, doi:10.1242/dev.025742 (2009).
24 Wang, S. *et al.* Trajectory Analysis Unveils Reelin's Role in the Directed Migration of Granule Cells in the Dentate Gyrus. *The Journal of Neuroscience* **38**, 137, doi:10.1523/JNEUROSCI.0988-17.2017 (2018).
25 Rickmann, M., Amaral, D. G. & Cowan, W. M. Organization of radial glial cells during the development of the rat dentate gyrus. *Journal of Comparative Neurology* **264**, 449-479, doi:10.1002/cne.902640403 (1987).
26 Barry, G. *et al.* Specific Glial Populations Regulate Hippocampal Morphogenesis. *The Journal of Neuroscience* **28**, 12328, doi:10.1523/JNEUROSCI.4000-08.2008 (2008).
27 Piper, M. *et al.* NFIA Controls Telencephalic Progenitor Cell Differentiation through Repression of the Notch Effector <em>Hes1</em&gt. *The Journal of Neuroscience* **30**, 9127 (2010).
28 Zhou, C.-J., Zhao, C. & Pleasure, S. J. Wnt Signaling Mutants Have Decreased Dentate Granule Cell Production and Radial Glial Scaffolding Abnormalities. *The Journal of Neuroscience* **24**, 121, doi:10.1523/JNEUROSCI.4071-03.2004 (2004).

29 Galichet, C., Guillemot, F. & Parras, C. M. Neurogenin 2 has an essential role in development of the dentate gyrus. *Development* **135**, 2031 (2008).
30 Frotscher, M., Haas, C. A. & Förster, E. Reelin Controls Granule Cell Migration in the Dentate Gyrus by Acting on the Radial Glial Scaffold. *Cerebral Cortex* **13**, 634-640, doi:10.1093/cercor/13.6.634 (2003).
31 Heng, Y. H. E., Heng, Y. H. E., Barry, G., Richards, L. J. & Piper, M. Nuclear Factor I Genes Regulate Neuronal Migration. *Neurosignals* **20**, 159-167, doi:10.1159/000330651 (2012).
32 Kang, P. *et al.* Sox9 and NFIA coordinate a transcriptional regulatory cascade during the initiation of gliogenesis. *Neuron* **74**, 79-94, doi:10.1016/j.neuron.2012.01.024 (2012).
33 Brunne, B. *et al.* Origin, maturation, and astroglial transformation of secondary radial glial cells in the developing dentate gyrus. *Glia* **58**, 1553-1569, doi:10.1002/glia.21029 (2010).
34 Scott, C. E. *et al.* SOX9 induces and maintains neural stem cells. *Nat Neurosci* **13**, 1181-1189, doi:10.1038/nn.2646 (2010).
35 Hashimoto, R. *et al.* Origins of oligodendrocytes in the cerebellum, whose development is controlled by the transcription factor, Sox9. *Mechanisms of Development* **140**, 25-40, doi:https://doi.org/10.1016/j.mod.2016.02.004 (2016).
36 Stolt, C. C. *et al.* The Sox9 transcription factor determines glial fate choice in the developing spinal cord. *Genes & Development* **17**, 1677-1689, doi:10.1101/gad.259003 (2003).
37 Tronche, F. *et al.* Disruption of the glucocorticoid receptor gene in the nervous system results in reduced anxiety. *Nature Genetics* (1999).
38 Takashima, Y. *et al.* Neuroepithelial Cells Supply an Initial Transient Wave of MSC Differentiation. *Cell* **129**, 1377-1388, doi:http://dx.doi.org/10.1016/j.cell.2007.04.028 (2007).
39 Wood, H. B. & Episkopou, V. Comparative expression of the mouse Sox1, Sox2 and Sox3 genes from pre-gastrulation to early somite stages. *Mechanisms of Development* **86**, 197-201, doi:https://doi.org/10.1016/S0925-4773(99)00116-1 (1999).
40 Akiyama, H., Martin, M.-C. C. J. F., Schedl, A. & CrombrugghE, B. d. The transcription factor Sox9 has essential roles in successive steps of the chondrocyte differentiation pathway and is required for expression of Sox5 and Sox6. *Genome Res* **12**, 47-56, doi:10.1101/ (2002).
41 Bernal, A. & Arranz, L. Nestin-expressing progenitor cells: function, identity and therapeutic implications. *Cellular and Molecular Life Sciences* **75**, 2177-2195, doi:10.1007/s00018-018-2794-z (2018).
42 Seymour, P. A. *et al.* SOX9 is required for maintenance of the pancreatic progenitor cell pool. *Proceedings of the National Academy of Sciences* **104**, 1865, doi:10.1073/pnas.0609217104 (2007).
43 Akiyama, H. *et al.* Essential role of Sox9 in the pathway that controls formation of cardiac valves and septa. *Proceedings of the National Academy of Sciences*

of the United States of America **101**, 6502, doi:10.1073/pnas.0401711101 (2004).

44 Reginensi, A. *et al.* SOX9 controls epithelial branching by activating RET effector genes during kidney development. *Hum Mol Genet* **20**, 1143-1153, doi:10.1093/hmg/ddq558 (2011).

45 Hodge, R. D. *et al.* Tbr2 is essential for hippocampal lineage progression from neural stem cells to intermediate progenitors and neurons. *The Journal of neuroscience : the official journal of the Society for Neuroscience* **32**, 6275-6287, doi:10.1523/JNEUROSCI.0532-12.2012 (2012).

46 Lavado, A., Lagutin, O. V., Chow, L. M. L., Baker, S. J. & Oliver, G. Prox1 Is Required for Granule Cell Maturation and Intermediate Progenitor Maintenance During Brain Neurogenesis. *PLOS Biology* **8**, e1000460, doi:10.1371/journal.pbio.1000460 (2010).

47 Roybon, L. *et al.* Neurogenin2 directs granule neuroblast production and amplification while NeuroD1 specifies neuronal fate during hippocampal neurogenesis. *PloS one* **4**, e4779-e4779, doi:10.1371/journal.pone.0004779 (2009).

48 Mimura-Yamamoto, Y. *et al.* Dynamics and function of CXCR4 in formation of the granule cell layer during hippocampal development. *Scientific Reports* **7**, 5647, doi:10.1038/s41598-017-05738-7 (2017).

49 Cahoy, J. D. *et al.* A Transcriptome Database for Astrocytes, Neurons, and Oligodendrocytes: A New Resource for Understanding Brain Development and Function. *The Journal of Neuroscience* **28**, 264 (2008).

50 Sugiyama, T., Osumi, N. & Katsuyama, Y. The germinal matrices in the developing dentate gyrus are composed of neuronal progenitors at distinct differentiation stages. *Developmental Dynamics* **242**, 1442-1453, doi:10.1002/dvdy.24035 (2013).

51 Takada, S. *et al.* Wnt-3a regulates somite and tailbud formation in the mouse embryo. *Genes & Development* **8**, 174-189 (1994).

52 Tien, A.-C. *et al.* Regulated temporal-spatial astrocyte precursor cell proliferation involves BRAF signalling in mammalian spinal cord. *Development* **139**, 2477, doi:10.1242/dev.077214 (2012).

53 Bayraktar, O. A., Fuentealba, L. C., Alvarez-Buylla, A. & Rowitch, D. H. Astrocyte development and heterogeneity. *Cold Spring Harbor perspectives in biology* **7**, a020362-a020362, doi:10.1101/cshperspect.a020362 (2014).

54 Takiguchi-Hayashi, K. *et al.* Generation of Reelin-Positive Marginal Zone Cells from the Caudomedial Wall of Telencephalic Vesicles. *The Journal of Neuroscience* **24**, 2286, doi:10.1523/JNEUROSCI.4671-03.2004 (2004).

55 Berger, O., Li, G., Han, S. M., Paredes, M. & Pleasure, S. J. Expression of SDF-1 and CXCR4 during Reorganization of the Postnatal Dentate Gyrus. *Developmental Neuroscience* **29**, 48-58, doi:10.1159/000096210 (2007).

56 Güven, A. *et al.* Extracellular matrix-inducing Sox9 promotes both basal progenitor proliferation and gliogenesis in developing neocortex. *eLife* **9**, e49808, doi:10.7554/eLife.49808 (2020).

57 Vong, K. I., Leung, C. K., Behringer, R. R. & Kwan, K. M. Sox9 is critical for suppression of neurogenesis but not initiation of gliogenesis in the cerebellum. *Mol Brain* **8**, 25, doi:10.1186/s13041-015-0115-0 (2015).

58 Martini, S. *et al.* A critical role for Sox9 in notch-induced astrogliogenesis and stem cell maintenance. *Stem Cells* **31**, 741-751, doi:10.1002/stem.1320 (2013).

59 Weider, M. & Wegner, M. SoxE factors: Transcriptional regulators of neural differentiation and nervous system development. *Seminars in Cell & Developmental Biology* **63**, 35-42, doi:https://doi.org/10.1016/j.semcdb.2016.08.013 (2017).

60 Shin, J. *et al.* Single-Cell RNA-Seq with Waterfall Reveals Molecular Cascades underlying Adult Neurogenesis. *Cell Stem Cell* **17**, 360-372, doi:10.1016/j.stem.2015.07.013 (2015).

61 Sun, W. *et al.* SOX9 Is an Astrocyte-Specific Nuclear Marker in the Adult Brain Outside the Neurogenic Regions. *The Journal of Neuroscience* **37**, 4493, doi:10.1523/JNEUROSCI.3199-16.2017 (2017).

62 Nagao, M., Ogata, T., Sawada, Y. & Gotoh, Y. Zbtb20 promotes astrocytogenesis during neocortical development. *Nature Communications* **7**, 11102, doi:10.1038/ncomms11102 (2016).

63 Glasgow, S. M. *et al.* Glia-specific enhancers and chromatin structure regulate NFIA expression and glioma tumorigenesis. *Nat Neurosci* **20**, 1520-1528, doi:10.1038/nn.4638 (2017).

64 Hasenpusch-Theil, K. *et al.* Transcriptional Analysis of Gli3 Mutants Identifies Wnt Target Genes in the Developing Hippocampus. *Cerebral Cortex (New York, NY)* **22**, 2878-2893, doi:10.1093/cercor/bhr365 (2012).

65 Namihira, M. *et al.* Committed Neuronal Precursors Confer Astrocytic Potential on Residual Neural Precursor Cells. *Developmental Cell* **16**, 245-255, doi:http://dx.doi.org/10.1016/j.devcel.2008.12.014 (2009).

66 Treves, A., Tashiro, A., Witter, M. P. & Moser, E. I. What is the mammalian dentate gyrus good for? *Neuroscience* **154**, 1155-1172, doi:https://doi.org/10.1016/j.neuroscience.2008.04.073 (2008).

67 Martin, L. A., Tan, S.-S. & Goldowitz, D. Clonal architecture of the mouse hippocampus. *The Journal of neuroscience : the official journal of the Society for Neuroscience* **22**, 3520-3530, doi:10.1523/JNEUROSCI.22-09-03520.2002 (2002).

68 Srinivas, S. *et al.* Cre reporter strains produced by targeted insertion of EYFP and ECFP into the ROSA26 locus. *BMC Developmental Biology* **1**, 4-4, doi:10.1186/1471-213X-1-4 (2001).

69 Livak, K. J. & Schmittgen, T. D. Analysis of Relative Gene Expression Data Using Real-Time Quantitative PCR and the 2−ΔΔCT Method. *Methods* **25**, 402-408, doi:https://doi.org/10.1006/meth.2001.1262 (2001).

70 Mikuni, T., Nishiyama, J., Sun, Y., Kamasawa, N. & Yasuda, R. High-Throughput, High-Resolution Mapping of Protein Localization in Mammalian Brain by In Vivo Genome Editing. *Cell* **165**, 1803-1817, doi:https://doi.org/10.1016/j.cell.2016.04.044 (2016).

Figure 1.

DG morphogenesis is differentially affected in *Sox1^{Cre}* versus *Sox9$^{fl/fl}$;Nestin-cre* mutants.

(A) H&E staining of 3-month-old (i-iii) and P2 (iv-vi) brain sections of *Sox9$^{fl/fl}$;Sox1$^{Cre/+}$* and *Sox9$^{fl/fl}$;Nestin-Cre* mutants compared to *Sox9$^{fl/+}$* controls. DG (outlined) appears smaller in *Sox9$^{fl/fl}$;Sox1$^{Cre/+}$* mutants compared to both controls and *Sox9$^{fl/fl}$;Nestin-Cre* mutants. **(B-C)** Quantification of DG surface as pixel area, in 3-month-old mice. (**B**) DG is significantly smaller in *Sox9$^{fl/fl}$;Sox1$^{Cre/+}$* mutants (33758±5898) compared to controls (55651±4492, P=0.0069, *t*-test) and *Sox9$^{fl/fl}$;Nestin-Cre* mutants (62994±3243, statistical analysis for *Nestin-Cre* mutants is not possible as n<3). The defect is already visible in P2 pups (**C**), when DG area is significantly smaller in *Sox9$^{fl/fl}$;Sox1$^{Cre/+}$* mutants (154949±22878) compared to controls (199203±5990, P=0.029), but not compared to *Sox9$^{fl/fl}$;Nestin-Cre* (176484±12459, P=0.277, Turkey's multiple comparison test, ANOVA P=0.035). **(D-F)** Immunofluorescence for YFP and SOX9 comparing respectively expression of *R26R^{eYFP}* reporter of Cre activity and SOX9 expression patterns in *Sox9$^{fl/fl}$;Sox1$^{Cre/+}$*, *Sox9$^{fl/fl}$;Nestin-Cre* mutants and controls, during forebrain (**D**) and archicortex (**E**) development. SOX9 remains expressed in *Nestin-Cre* mutants in both the CH and DNE (white asterisks in D). Yellow dashed square in (**D**) indicate area showed in (**E**) at higher magnification, also schematized in (**F**). Signal from SOX9 immunofluorescence in *Sox9* mutant tissue was confirmed to be background with ISH for *Sox9* (Fig. S.2)

LV: lateral ventricle; DT: dorsal telencephalon; ARK: archicortex; CH; cortical hem; DNE: dentate neuroepithelium. Scale bar represent 400µm in A(i-iii); 200µm in A(iv-vi) and (D); 50µm in (E).

Figure 2.

Granule neuron progenitors are generated normally but their distribution in SOX9 mutant developing DG is abnormal.

(A-D) Immunofluorescence for TBR2 (**A**) and PROX1 (**C**) were performed at indicated developmental (E14.5: Ai, ii; E16.5: Ci, ii; E18.5: Aiii-v and Ciii-v) and postnatal stages (P2: Avi-viii and Cvi-viii) of DG development. Arrows in Aiv-v, vii-viii and Cvii-viii point to respectively TBR2+ and PROX1+ cells accumulating close to the ventricle (yellow

dashed line). The three matrices are delineated (Aiii-viii and Cvi-viii). Quantification showing a reduced number of TBR2+ cells at P2 (**B**) in *Sox9$^{fl/fl}$;Sox1$^{Cre/+}$* mutants (2041.67+323.72; P=0.03380 Dunn's multiple comparison test; Kruskal-Wallis test P=0.0107) compared to controls (2792±331.72 TBR2+ cells). The same tendency was observed in P2 *Sox9$^{fl/fl}$;Nestin-Cre* mutants (**B**) (2329.67±137.19 TBR2+ cells), and for PROX1+ cells (**D**) at P2 in both mutants *(Sox9$^{fl/fl}$;Sox1^{Cre}*: 2156.67±325.41 and *Sox9$^{fl/fl}$;Nestin-Cre* :2384.00±173.25) compared to controls (2895.33±367.51), although this did not reach statistical significance. **(E)** Analysis of TBR2+ progenitors and PROX1+ granule neurons distribution along the three matrices, according to the scheme where dashed lines indicate areas considered for 1ry, 2ry and 3ry matrix quantification (also show in Aiii-viii and Cvi-viii). At E18.5 (***i***), more TBR2+ cells were found in the 2ry matrix of *Sox9$^{fl/fl}$;Nestin-Cre* mutants (276.53±18.96) compared to both *Sox9$^{fl/fl}$;Sox1$^{Cre/+}$* mutants (207.33±39.85, P=0.03660) and controls (180.07±1.79, P=0.00850, Turkey's multiple comparison test, ANOVA P=0.0090), while less TBR2+ cells were found in the 3ry matrix of both *Sox9$^{fl/fl}$;Sox1$^{Cre/+}$* mutants (66.93±7.90, P=0.0016) and *Sox9$^{fl/fl}$;Nestin-Cre* mutants (84.00±8.50, P=0.0075) compared to controls (132.53±18.29, Turkey's multiple comparison test, ANOVA P=0.0017). At P2 (***ii***) more TBR2+ cells are found in 1ry matrix of *Sox9$^{fl/fl}$;Sox1$^{Cre/+}$* mutants (79.47+14.59), compared to controls (36.47±9.87, P=0.0101) and *Sox9$^{fl/fl}$;Nestin-Cre* mutants (48.13±10.35, P= 0.0399, Turkey's multiple comparison test, ANOVA P=0.0106). In *Sox9$^{fl/fl}$;Nestin-Cre* mutants, more TBR2+ cells are accumulating in the 2ry matrix (184.07±8.47) compared to *Sox9$^{fl/fl}$;Sox1$^{Cre/+}$* mutants (127.87±22.72, P=0.0175, Turkey's multiple comparison test, ANOVA P=0.0183). In both *Sox9* mutants, less TBR2+ cells are found in the 3ry matrix (*Sox9$^{fl/fl}$;Sox1$^{Cre/+}$*: 201.00±59.44, P=0.0119; *Sox9$^{fl/fl}$;Nestin-Cre*: 233.73±27.81, P=0.029) compared to controls (378.93±57.88, Turkey's multiple comparison test, ANOVA P=0.0109). At P2, PROX1+ cells (***iii***) accumulate in the 1ry matrix of *Sox9$^{fl/fl}$;Sox1$^{Cre/+}$* mutants, (111.00±39.89) compared to controls (17.67±14.15, P=0.0088, Turkey's multiple comparison test, ANOVA P=0.0100), and a significant decrease in the 3ry matrix of both *Sox9$^{fl/fl}$;Sox1$^{Cre/+}$* mutants (1786.67±266.25, P=0.0117) and *Sox9$^{fl/fl}$;Nestin-Cre* mutants (1991.33±260.48, P=0.0329) is observed compared to controls (2758.33±297.16, Turkey's multiple comparison test, ANOVA P=0.0112). **(F)** Analysis of the distribution of PROX1+ granule neurons distribution within the upper and lower blade of the forming DG at E18.5: the 3ry matrix was divided in 10 horizonal ventral to

dorsal bins spanning the lower to upper blade domain. Cells were then counted within each bin. The percentage of PROX1+ cells present in each bin is represented. In *Sox9*$^{fl/fl}$*;Sox1*$^{Cre/+}$ mutants, PROX1+ cells are accumulating in the lower blade (18.40±2.29%) compared to controls (13.57±1.29%, P=0.0187), and are reduced in the upper blade (8.57±0.58%) compared to controls (13.13±0.55%, P=0.0071, Turkey's multiple comparison test, Two way ANOVA interaction P=0.0387, row factor P<0.0001, column factor P=0.9991). A similar tendency was observed in *Sox9*$^{fl/fl}$*;Nestin-Cre* mutants, however it did not reached statistical significance.
DG: dentate gyrus; DNE: dentate neuroepithelium. Scale bar represent 50µm in A(i,ii); 100µm in A(iii-viii) and B(i-v); 200µm in B(vi-viii).

Figure 3.

Ectopic accumulation of neuronal progenitors close to the ventricle suggests migratory defects in *Sox9* mutant DG.

(A) Triple immunostaining for TBR2, SOX2 and EdU at P2. EdU was injected at E18.5. Insets show higher magnification of cells in ectopic cluster (schematized in **B**), magnified area is indicated by the white arrow. Yellow and pink arrowheads indicate respectively TBR2+EdU+ and SOX2+EdU+ cells in the ectopic cluster. **(B)** Illustration showing location of ectopic cluster within the developing DG. **(C-D)** Immunofluorescences for the differentiation markers PROX1 (**C**) and NeuroD1 (**D**) in *Sox9*$^{fl/fl}$*;Sox1*$^{Cre/+}$ and *Sox9*$^{fl/fl}$*;Nestin-Cre* mutants compared to controls at P2 (**C**) and E18.5 (**D**), respectively. Both markers are expressed by cells within the ectopic cluster (arrows) in *Sox9* mutants**. (E)** Quantification of ectopic cluster size at E18.5 and P2 in *Sox9*$^{fl/fl}$*;Sox1*$^{Cre/+}$ compared to *Sox9*$^{fl/fl}$*;Nestin-Cre* mutants. The percentage of TBR2+ progenitors in ectopic cluster relative to total number of TBR2+ progenitors in 2ry matrix is represented. At E18 (***i***), the ectopic cluster size was comparable between *Sox9*$^{fl/fl}$*;Sox1*$^{Cre/+}$ (34.11±2.35%) and *Sox9*$^{fl/fl}$*;Nestin-Cre* mutants (28.41±3.10%). It then significantly decreases in *Sox9*$^{fl/fl}$*;Nestin-Cre* mutants at P2 compared to E18.5 (17.87±3.41%, P=0.0172, *t* test) and *Sox9*$^{fl/fl}$*;Sox1*$^{Cre/+}$ at the same stage (36.73±5.30%, P=0.0061, *t* test). In agreement with the smaller ectopic matrix size at P2, less newly formed TBR2+EdU+ progenitors (***ii***) were found in the ectopic cluster of *Sox9*$^{fl/fl}$*;Nestin-Cre* mutants (18.90±3.53%) compared to *Sox9*$^{fl/fl}$*;Sox1*$^{Cre/+}$ (40.13±6.97%, P=0.0084 *t* test). **(F)** Schematic of *in utero* electroporation protocol. **(G)**

Immunostaining for PROX1 and dsRed live fluorescence. Double positive cells from the dashed yellow square are showed at higher magnification in the inset. **(H)** The total number of dsRed+ cells was significantly smaller in *Sox9*$^{fl/fl}$*;Sox1*$^{Cre/+}$ mutants (153.60±33.72) compared to controls (583.40±243.76, P=0.0045 *t* test). **(I)** The proportion of dsRed+ on total PROX1+ cells was not significantly reduced in *Sox9* mutants (16.40±15.11%) compared to controls (33.40±7.27%). **(J)** Distribution of dsRed+ cells along the three matrices (as schematized in Fig. 2.D). We observed more dsRed+ cells in the 1ry matrix of *Sox9*$^{fl/fl}$*;Sox1*$^{Cre/+}$ mutants compared to controls (31.33±7.47% vs. 14.32±7.03%, P=0.0105 *t* test) and less in the 3ry matrix (29.49±11.13% vs. 51.27±14.20%, P=0.0287 *t* test).
DNE: dentate neuroepithelium; IUE: *in utero* electroporation. Scale bars represent 100µm.

Figure 4.

Glial scaffold formation and astrocytic progenitor emergence are delayed in *Sox9* mutants according to levels of Cre activity in CH.

(A-C) Analysis of glial scaffold formation. **A)** Immunofluorescence for GFAP at E18.5 (Ai-iii) and P2 (Aiv-vi) showing GFAP reduction in both mutants at E18.5. Dashed line delineates the developing DG area, yellow dashed squares indicate areas magnified in insets. **B)** Representation of the glial scaffold (red lines) in DG. **C)** GFAP immunofluorescence quantification (pixel area). At E18.5, GFAP expression was significantly reduced in *Sox9*$^{fl/fl}$*;Sox1*^{Cre} mutants (18537.49±6990.47) compared to controls (3859.45±2347.25, P=0.0289), while quantification in *Sox9*$^{fl/fl}$*;Nestin-Cre* did not reach statistical significance (7465.87±4875.50, P=0.0836, Turkey's multiple comparison test, ANOVA P=0.0292). At P2, GFAP expression is recovered in both *Sox9* mutants compared to controls. **(D)** Double immunostaining for ALDH1L1 and GFAP in wild type at E18.5, E16.5 and E13.5. ALDH1L1 and GFAP are co-expressed at E18.5 in the fimbria (**b** insets on the right) but not around the forming DG (**a** insets on the right). Earlier, ALDH1L1, but not GFAP, is expressed in a similar pattern, in the fimbria and in a few cells around the forming DG (arrow in Dii), as early as E13.5 in the archicortex (arrow in Diii). **(E)** Double immunostainings for SOX2;LEF1 and SOX2;ALDH1L1 at E13.5. SOX2 and LEF1 mutually exclusive expression patterns delineate the LEF1-SOX2^{high} CH and LEF1+SOX2^{low} DNE. ALDH1L1+ cells are

exclusively located in the SOX2^{high} CH. **(F-G)** Immunostaining (**F**) and quantification (**G**) of ALDH1L1+ cells in *Sox9* mutants at E13.5 (i-iii) and E16.5 (iv-vi) compared to controls. White arrows in Fv indicate rare ALDH1L1+ cells found in *Sox9$^{fl/fl}$;Sox1^{Cre}* mutants. The number of ALDH1L1+ cells was significantly reduced in *Sox9$^{fl/fl}$;Sox1^{Cre}* mutants compared to controls, both at E13.5 (4.43±3.93 vs. 14.14±4.58, P=0.0193) and E16.5 (15.58±1.62 vs. 39.54±7.27, P=0.0338), while it was unaffected in *Sox9$^{fl/fl}$;Nestin-Cre* mutants (E13.5: 11.00±2.29, P=0.5373, E16.5: 43.73±13.00, P=0.8288, Turkey's multiple comparison test, ANOVA P=0.0242 and P=0.0147). **(H)** Analysis of *Aldh1l1* expression levels by qPCR from dissected DT and ARK of E12.5 *Sox9$^{fl/fl}$;Sox1^{Cre}, Sox9$^{fl/fl}$;Nestin-Cre* and control embryos. *Aldh1l1* expression was significantly reduced in the ARK of *Sox9$^{fl/fl}$;Sox1^{Cre}* compared to both controls (P=0.0028) and *Sox9$^{fl/fl}$;Nestin-Cre* mutants (P=0.0047, Turkey's multiple comparison test, ANOVA P=0.0021). **(I)** Triple immunostaining for YFP, SOX9 and ALDH1L1 at E13.5 (i,ii,v,vi) and E16.5 (ii,iv,vii,viii) in *Sox9$^{fl/fl}$;Sox1^{Cre}* and *Sox9$^{fl/fl}$;Nestin-Cre* mutants. A few double positive SOX9;ALDH1L1 cells are detected in the CH of both *Sox9* mutants (white arrows). More of these are present in *Sox9$^{fl/fl}$;Nestin-Cre* compared to *Sox9$^{fl/fl}$;Sox1^{Cre}* mutants due differential Cre activity as shown by the *R26R^{eYFP}* reporter expression.

LV: lateral ventricle; DNE: dentate neuroepithelium; CH: cortical hem; DT: dorsal telencephalon; ARK: archicortex. Scale bars represent 200µm in A; 100µm in B; 50µm in D, F, H and I.

Figure 5.

CH-specific deletion of *Sox9* using *Wnt3a^{iresCre}* compromises glial scaffold formation exclusively within the fimbria.

(A-D) Analysis of *Wnt3a^{iresCre}* recombination pattern in the archicortex. **(A)** Double immunofluorescence for LEF1 and YFP in *Wnt3a$^{iresCre/+}$;R26^{ReYFP}* embryos at E12.5. Cells that have undergone Cre recombination are mostly observed in the LEF1- CH but a few YFP+ cells are seen the LEF1+ DNE (arrowheads in magnified inset). **(B)** Double immunofluorescences for PROX1;YFP (Bi-iii) and GFAP;YFP (Biv,ix) in P2 *Wnt3a$^{iresCre/+}$;R26R^{eYFP}* embryos in the area schematized in **(C)**. Insets on the right are magnified areas from yellow dashed boxes on the left. Cells that have undergone Cre recombination are mostly GFAP+ and PROX1-, in agreement with a CH specific

recombination pattern (Bi-iii). Arrowheads in Bi-iii and insets indicate some rare YFP+PROX1+ cells in the DG representing 6.45±1.00% of PROX1+ cells **(D)**. Arrows and arrowheads in Biv,ix and insets indicates respectively YFP-GFAP+ and YFP+GFAP+ fibers in the DNE/fimbria (Biv-vi) and around the DG (Bvii-ix), indicating the GFAP+ glial scaffold around the DG only partially originate from the CH. **(E-F)** Quantification and immunostainings for YFP (Fi,ii); SOX9 (Fiii,iv); ALDH1L1 (Fv,vi) at E13.5 and GFAP at E18.5 in *Sox9*$^{fl/fl}$*;Wnt3a*$^{iresCre/+}$ mutant compared to controls. In E13.5 archicortices of *Sox9*$^{fl/fl}$*;Wnt3a*$^{iresCre/+}$ mutant and control embryos the CH specific deletion of SOX9 is confirmed. The number of ALDH1L1+ cells is significantly reduced (**E**) in *Sox9*$^{fl/fl}$*;Wnt3a*$^{iresCre/+}$ mutants (6.95±2.56) compared to controls (14.14±4.58, P=0.022 *t* test). At E18.5, the GFAP+ glial scaffold is affected exclusively within the fimbria (star in Fviii) and not around the DG (arrowheads in Fvii-viii).
CH: cortical hem; DNE: dentate neuroepithelium. Scale bars represent 100µm in A and F(vii-viii) and 50µm in B, F(i-vi).

Figure 6.

CH-specific deletion of *Sox9* using *Wnt3a*^{iresCre} specifically affects granule neuron progenitor migration along the 1ry-to-3ry matrix axis.

(A-C) Analysis of PROX1+ differentiating granule neurons at E18.5 *Sox9*$^{fl/fl}$*;Wnt3a*$^{iresCre/+}$ DG. **A)** Immunostaining for PROX1. The total number of PROX1+ cells (**B**) and their distribution between upper and lower blade of the forming DG (**C**, see Fig. 3.E for analysis settings) was not affected in *Sox9*$^{fl/fl}$*;Wnt3a*$^{iresCre/+}$ mutants compared to controls. **(D-G)** Analysis of TBR2+ intermediate progenitors at E18.5 in *Sox9*$^{fl/fl}$*;Wnt3a*$^{iresCre/+}$ DG via immunofluorescence (**D**). The total number of TBR2+ cells is unchanged (**E**) but their distribution along the three matrices (**F**) is affected as there were more cells in the 2ry matrix of *Sox9*$^{fl/fl}$*;Wnt3a*$^{iresCre/+}$ mutants (228.60±5.37) compared to controls (180.07±1.79, P=0.0001, *t* test). Arrow indicates accumulation of TBR2+ cells in the ectopic cluster in *Sox9*$^{fl/fl}$*;Wnt3a*$^{iresCre/+}$ mutants. **G)** Percentage of TBR2+ in ectopic cluster. The percentage of TBR2+ cells in the ectopic cluster is comparable to that observed *Sox9*$^{fl/fl}$*;Sox1*$^{Cre/+}$ and *Sox9*$^{fl/fl}$*;Nestin-Cre* mutants (calculated as % of TBR2+ progenitors in ectopic cluster relative to total number of TBR2 progenitors in 2ry matrix). **(H)** Immunofluorescence for NeuroD1 showing ectopic differentiation towards granule neuron cell fate in the ectopic cluster of

Sox9$^{fl/fl}$*;Wnt3a*$^{iresCre/+}$ mutants (arrow). **(I)** Triple immunostaining for SOX9, YFP and GFAP showing YFP- cells accumulating next to the SOX9+ DNE in E18.5 *Sox9*$^{fl/fl}$*;Wnt3a*$^{iresCre/+}$*;R26R*^{eYFP} mutants (delineated by yellow dashed line) and underlaid by a defective GFAP scaffold.
DNE: dentate neuroepithelium. Scale bars represent 50µm in A, B(i,ii) and L; 100µm in B(iii,iv), D, G, and J.

Figure 7.

Model for the dual origin and function of the DG glial scaffold based on the analysis of defects following differential deletion of *Sox9*.

(A-D) Schematic of mouse models used for *Sox9* conditional deletion and analysis of DG development. The pattern of Cre recombination is represented in the archicortex at E13.5 (green area) and the corresponding phenotype observed at E18.5/P2. Stars indicate local absence of the GFAP+ glial scaffold. **(E)** Figure legend. **(F)** Model of DG development based on defects observed following differential deletion of *Sox9*. At early stages of DG development (E13.5), granule neuron progenitors undergo delamination from the 1ry matrix and form the 2ry matrix (migration direction depicted by arrow **1**). This initial step is hypothesized to be independent of the glial scaffold because it is not affected in its absence in *Sox9* mutants. From E18.5, progenitor migration towards the forming DG/3ry matrix relies on the fimbrial scaffold (red lines, arrow **2**). This fimbrial scaffold derives from astrocytic progenitors located in the CH (red area). At the same time, the dentate scaffold around the DG (blue lines) provides support for granule neuron positioning within upper and lower blades of the forming DG (arrows **3**). Cells giving rise to this second scaffold are DNE derived (blue area).

Figure S.1

Absence of SOX9 expression in a 2 months-old *Sox9*$^{fl/fl}$*;Nestin-Cre* mutant brain.

Immunofluorescence for SOX9 was performed to confirm absence of SOX9 expression in the brain of adult *Sox9*$^{fl/fl}$*;Nestin-Cre* mutants (ii, iv) compared to controls (i, iii).
LV: lateral ventricle; CC: corpus callosum. Scale bars represent 100µm.

Figure S.2

Qualitative and quantitative analyses of *Sox9* transcripts confirm residual *Sox9* expression in embryonic *Sox9*$^{fl/fl}$*;Nestin-Cre* forebrains.

(A) Analysis of *Sox9* expression by *ISH* confirms ventral to dorsal activity of *Nestin-Cre* as *Sox9* is still expressed in the DT at E11.5 in *Sox9*$^{fl/fl}$*;Nestin-Cre* mutants, (iii) and in the most ventral part of the ARK at E12.5 and E13.5 (arrows in vi, ix). Some rare cells still express *Sox9* in the archicortex of *Sox9*$^{fl/fl}$*;Sox1*$^{Cre/+}$ mutants (arrow in v, viii). **(B)** Quantification of *Sox9* expression via qPCR from dissected DT and ARK of controls, *Sox9*$^{fl/fl}$*;Sox1*$^{Cre/+}$ and *Sox9*$^{fl/fl}$*;Nestin-Cre* E12.5 embryos. *Sox9* expression is drastically reduced in both DT and ARK of *Sox9*$^{fl/fl}$*;Sox1*$^{Cre/+}$ compared to controls (*Sox9* fold change in DT: 0.006±0.008, P<0.0001; and ARK: 0.027±0.014, P<0.0001 Turkey's multiple comparison test; ANOVA P<0.0001). *Sox9* expression was also significantly reduced in *Sox9*$^{fl/fl}$*;Nestin-Cre* mutants compared to controls (*Sox9* fold change in DT: 0.204±0.08, P=0.0002; and ARK: 0.234±0.147, P=0.0017 Turkey's multiple comparison test; ANOVA P=0.0005). *Sox9* tended to be present at higher levels in *Sox9*$^{fl/fl}$*;Nestin-Cre* compared to *Sox9*$^{fl/fl}$*;Sox1*$^{Cre/+}$, which may reflect differences in Cre activities, however this was not statistically significant.
LV: lateral ventricle; DT: dorsal telencephalon; ARK: archicortex; CH; cortical hem; DNE: dentate neuroepithelium. Scale bars represent 200µm.

Figure S.3

***Sox9* deletion is not associated with increased cell death in the developing DG.**

(A) Immunofluorescence for cleaved Caspase-3 at consecutive stages of DG development (E16.5: i, ii; E18.5: iii, iv; P2: v, vi) in *Sox9*$^{fl/fl}$*;Sox1*$^{Cre/+}$ mutants compared to controls. **(B)** Quantification of cleaved Caspase-3+ cells in 1ry and 2ry matrix of P2 *Sox9*$^{fl/fl}$*;Sox1*$^{Cre/+}$ mutants compared to controls
DNE: dentate neuroepithelium. Scale bars represent 100µm.

Figure S.4

***Sox9* deletion does not alter neural progenitor emergence or differentiation towards a granule neuron fate.**

(A-D) DG progenitors EdU birth-dating experiment. **A)** Double staining for TBR2 and EdU. Arrows indicate accumulation of cells close to the ventricle in *Sox9* mutants. **B)** Experimental protocol: EdU was injected at E18.5, samples harvested at P2 and immunostained for TBR2 and EdU. **C)** TBR2+ progenitor emergence, quantified as the percentage of TBR2+EdU+/TBR2, was not affected by *Sox9* deletion. **D)** Distribution of newly generated TBR2+EdU+ progenitor along the three matrices (as delineated in Ai). A significant accumulation of TBR2+EdU+ newly formed progenitors was observed in the 1ry matrix of *Sox9*$^{fl/fl}$*;Sox1*$^{Cre/+}$ mutants (26.87±5.12) compared to controls (9.20±4.30, P=0.0169), while *Sox9*$^{fl/fl}$*;Nestin-Cre* mutants were not affected (15.93±6.60, Turkey's multiple comparison test, ANOVA P=0.0197). **(E-G)** Granule neurons EdU birth-dating experiment. **E)** Double staining for PROX1 and EdU. **F)** EdU was injected at E16.5, which corresponds to the first stage when this cell type appears in the developing DG, and samples harvested at E18.5. **G)** The proportion of PROX1+EdU+/PROX1+ newly formed granule neurons is unchanged between controls and both *Sox9* mutants, indicating that *Sox9* deletion is not affecting granule neuron differentiation.
Scale bars represent 100µm.

Figure S.5

***In utero* electroporation does not compromise cell survival in the developing dentate gyrus of *Sox9* mutants.**

Immunostaining for cleaved Caspase-3 in P2 *Sox9*$^{fl/fl}$*;Sox1*$^{Cre/+}$ pups and controls after IUE at E15.5, comparing ipsi- (in controls ***i*** and in mutants ***ii***) and contra-lateral (in mutants ***iii***) hemispheres to the injection, showing that cell death is not increased in *Sox9* mutants after IUE. Insets showing higher magnification of Cleaved Caspase-3 expressing cells in ectopic cluster.
IUE: *in utero* electroporation; DNE: dentate neuroepithelium; ipsi: ipsilateral to injection; contra: contralateral to injection. Scale bars represent 100µm.

Figure S.6

Migratory clues secreted by Cajal-Retzius cells and required during DG development are not affected in *Sox9* mutants.

(A) Analysis by qPCR of the expression of secreted chemokines *Reln*, *Cxcl12* and their receptors *Vlvdr*, *Cxcr4*. mRNA was extracted from E12.5 dissected archicortices of *Sox9*$^{fl/fl}$*;Sox1*$^{Cre/+}$, *Sox9*$^{fl/fl}$*;Nestin-Cre* and control embryos. No significant difference was found in any of the genes analyzed in both *Sox9* mutants compared to controls. **(B)** Immunofluorescence for REELIN at E18.5. The expression pattern and intensity of REELIN staining appeared unaffected in both *Sox9* mutants compared to controls. Scale bars represent 100µm.

Figure S.7

Early CNS-specific deletion of *Sox9* does not affect NF1A/B expression in the forebrain.

(A) Immunofluorescence for NF1A at E12.5. Levels of expression appear similar in both DT and ARK in *Sox9* mutants compared to controls. **(B)** Quantification of *Nfia/b* expression levels by qPCR in dissected dorsal telencephalons and archicortices at E12.5. There is no significant difference in *Nfia/b* levels in *Sox9* mutants compared to controls.
LV: lateral ventricle; DT: dorsal telencephalon; ARK: archicortex. Scale bar represent 200µm in A(i-ii) and 100µm in A(iii-iv).

Figure S.8

PROX1+ granule neurons distribution in the 3ry matrix is not affected in *Sox9*$^{fl/fl}$*;Wnt3a*$^{iresCre/+}$ mutants.

Percentage of PROX1+ granule neurons positioned in the DG lower blade (bins 1 to 5), versus the DG upper blade (bins 6 to 10) in controls, *Sox9*$^{fl/fl}$*;Sox1*$^{Cre/+}$ and *Sox9*$^{fl/fl}$*;Nestin-Cre* mutants (results from Fig. 2.F), and *Sox9*$^{fl/fl}$*;Wnt3a*$^{iresCre/+}$ mutants (results from Fig. 6.C) at E18.5. In contrast with *Sox9*$^{fl/fl}$*;Sox1*$^{Cre/+}$ and *Sox9*$^{fl/fl}$*;Nestin-Cre* mutants, PROX1+ granule neurons are distributed normally in *Sox9*$^{fl/fl}$*;Wnt3a*$^{iresCre/+}$ mutants.

MATERIAL AND METHODS:

Mouse strains, husbandry and genotyping

All experiments carried out on mice were approved under the UK Animal (scientific procedures) Act 1986 (Project license n. 80/2405). Mouse husbandry, breeding, ear biopsies and vaginal plug (VP) checks were performed by the Biological Research Facility team of the Francis Crick Institute. Animals were kept in individually ventilated cages (ICV) with access to food and water ad libitum. The VP day was considered as 0.5 day from time of conception (E0.5) and the day of birth termed P0.

All mouse lines used were previously described: *Sox9*$^{fl/fl}$ conditional targeted mutation, MGI: 2429649[40]; *Sox1*$^{Cre/+}$ targeted mutation, MGI: 3807952[38]; *Nestin-Cre* transgenic mutation, MGI: 2176173[37]; *Wnt3a*$^{IRES\text{-}Cre}$ targeted mutation, MGI: 98956[21]; *R26R*^{eYFP} targeted mutation, MGI: 2449038[68]. To obtain *Sox9* conditional mutations, *Sox9*$^{fl/fl}$ mice were crossed with either *Sox1*$^{Cre/+}$, *Nestin-Cre* or *Wnt3a*$^{IRES\text{-}Cre}$ mice. All Cre lines were kept in heterozygosity. To verify Cre recombination pattern, *R26R*^{eYFP} reporter allele was also present in all samples analysed, even when not indicated. Genotyping of embryos and adult mice was performed by Transnetyx.

EdU injection

For cell birth-dating experiments, 10mg/ml EdU solution, from Click-iT™ EdU imaging kit, was injected intraperitoneally in pregnant females at a dose of 30µg/g body weight. Injection was performed at either E16.5 or E18.5 stage of pregnancy and samples collected at E18.5 or P2 respectively. Schematic of protocols in Fig. S.4.B,F.

Tissue harvesting and staining

Pregnant females were killed by cervical dislocation, embryonic heads were dissected out in chilled PBS and fixed by immersion in chilled 4% PFA at 4°C for 1 to 2 hours. From E16.5 onwards, brains were dissected out of the skull before fixation. P2 pups were killed by cervical dislocation, brains were dissected out on chilled PBS and fixed by immersion in chilled 4% PFA at 4°C for 2 hours. After fixation, embryonic brains were washed once in PBS, cryopreserved in sucrose 30%, then embedded in OCT, frozen on dry ice and stored at -80°C. Samples were cryosectioned at 14µm and sections placed on Superfrost Plus glass slides, air dried for 5 minutes, washed twice

in PBS for 5 minutes. For some antibodies (listed in Table 1), antigen retrieval was performed immerging slides in 10% target retrieval solution pH6.1 diluted 1:10 in distilled water, for 30 minutes at 65°C or 15 minutes at 95°C, then washing twice in PBS for 10 minutes. Slides were then incubated in a humidified chamber in blocking solution (10% donkey serum in 0.1% triton X-100 PBS) for at least 30 minutes, then incubated overnight at 4°C with primary antibodies diluted in blocking solution (dilution indicated in Table 1). The following day, sections were washed twice for 5 minutes in 0.1% triton X-100 PBS, incubated with secondary antibodies (Table 2) and DAPI diluted in blocking solution for 2 hours at room temperature in a dark humified chamber. Finally, sections were washed again twice for 5 minutes in PBS, briefly in distilled water, air dried and coverslip mounted with Aqua-poly/Mount. Apoptosis detection with terminal deoxynucleotidyl transferase dUTP nick end labelling (TUNEL) assay was performed using the ApopTag® Red *In Situ* Apoptosis Detection Kit, following manufacturer's instructions, after secondary antibody incubation. Detection of DNA-incorporated EdU was performed using Click-iT™ EdU imaging kit, following manufacturer's instructions, after secondary antibody incubation.

For hematoxylin and eosin (H&E) staining, pregnant females and adult mice were killed by cervical dislocation, embryonic and adult brains were dissected out in chilled PBS, fixed overnight in Bouin's solution at 4°C, washed twice for 10 minutes in 70% ethanol and stored in 70% ethanol until processing. Samples were embedded in wax, sectioned at 4µm and stained by the Francis Crick Institute Experimental Histopathology facility.

In situ hybridization probe formation and staining

Digoxigenin (DIG)-tagged antisense RNA probes were made from an ampicillin-resistant plasmid (kindly gifted by Dr. Paul Sharp) containing *Sox9* cDNA followed by a T7 promoter. Plasmid was amplified with *E. Coli* culture and purified with NucleoBond Xtra Midi plus kit. 5µl of plasmid (corresponding to 5-10µg) was linearized with 1µl of SmaI enzyme, 2ul of 10x SmartCut buffer and 12ul of RNase free water and confirmed with 1% agarose gel electrophoresis. Linearized plasmids were purified by phenol-chloroform extraction and precipitated by adding 1µl glycogen, 1/20 of sodium acetate 3M and equal volume of 100% ethanol, incubated at -20°C for 1 hour. The precipitate was recovered by centrifugation at 13000 RPM at 4°C for 15min, air

dried and resuspended in 16µl of RNase free water. For DIG-tagged probes synthesis, 1µl linearized plasmid, 1X transcription buffer, 2µl of DIG-tagged nucleotides, 1µl T7 RNA polymerase, 0.5µl RNase inhibitor, 1µl DTT 100mM and 11.5µl of RNase free water were incubated at 37°C for 2 hours. Probe formation was confirmed with 1% agarose gel electrophoresis. Probes were precipitated by adding 1µl glycogen, 8µl lithium chloride 5M, 2/3 of final volume of 100% ethanol and 1/3 of final volume of RNase free water, incubated at -80°C for 30 minutes. Precipitates were recovered by centrifugation at 13000 RPM at 4°C for 15 minutes, then washed in 70% ethanol (v/v) centrifuged at 13000 RPM for 15min at 4°C. Pellet containing the RNA probes were then air-dried at 37°C and resuspended in 50-100µl of ISH hybridization buffer (50% (v/v) deionised formamide, 4X SSC, 0.01M β-mercaptoethanol, 10% dextran sulphate, 2X Denhart's solution, 0.23mg/ml yeast t-RNA diluted in RNase free water).

For *in situ* hybridisation (*ISH*) staining, cryosections were initially air-dried, washed twice for 5 minutes in PBS, fixed 30 minutes with 4% PFA at room temperature in a humidified chamber, washed twice for 10 minutes in PBS, and incubated in pre-hybridization buffer (50% (v/v) deionised formamide, 1X saline-sodium citrate (SSC) diluted in RNase free water) for 1 hour in a 65°C waterbath. For each slide, 1µl of RNA probe was denaturated in 200µl hybridization buffer for 10 minutes at 70°C, then applied on sections. Hybridization was carried out in a humidified chamber overnight in a 65°C water bath. The following day, sections were washed twice for 15 minutes, and once for 30 minutes with pre-warmed washing buffer (50% (v/v) deionised formamide, 1X SSC, 0.1% (v/v) Tween 20 diluted in MilliQ water) at 65°C, then twice for 30 minutes with MABT (20mM Maleic acid, 30mM sodium chloride (NaCl), 0.02% (v/v) Tween 20, adjusted to pH7.5 and diluted in MilliQ water) at room temperature. Sections were then incubated in a humidified chamber at room temperature for 1 hour in blocking buffer (10% (v/v) sheep serum, 2% (v/v) blocking reagent diluted in MABT), then overnight in anti-DIG coupled to alkaline phosphatase antibody (α-DIG-AP) diluted 1:1500 in blocking buffer. The following day, sections were washed four times for 20 minutes at room temperature with MABT then twice for 10 minutes in pre-staining solution (100mM NaCl, 50mM magnesium chloride (MgCl2), 100mM Tris-HCl pH9.5, 1% (v/v) Tween 20 in MilliQ water). Alkaline phosphatase staining was then performed incubating slides with staining solution (pre-staining solution plus 5% (w/v) Polyvinyl alcohol (PVA), 4.5µl of Nitrotetrazolium Blue chloride (NBT) and 3.5µl of 5-

bromo-4-chloro-3-indolyl-phosphate (BCIP) per ml of staining solution) for 1 hours to 2 days at 37°C in a dark chamber. Once the desired staining intensity was reached, the reaction was stopped washing sections twice for 10 minutes in 0.1% triton X-100 PBS. Finally, sections were fixed for 10 minutes in 4% PFA, washed twice for 5 minutes in PBS then briefly in distilled water, air-dried, and coverslip mounted with Aqua-poly/Mount.

Quantitative PCR and analysis

For gene expression analysis, E12.5 embryos were dissected in sterile PBS, dorsal telencephalon and archicortex were separately snap-frozen in liquid nitrogen. RNA was extracted with the RNeasy Plus Micro kit, following manufacturer's instructions. Complimentary (c) DNA was synthetized from 250ng of extracted RNA in 1X qScript cDNA SuperMix diluted in RNase free water and incubated on the Tetrad 2 Thermal Cycler following the indicated reverse transcription protocol. Resulting cDNA was diluted in RNase free water at a final concentration of 200µg/µl. Transcripts were quantified with quantitative PCR (qPCR), mixing 800µg of cDNA in 1X ABsolute QPCR SYBR Green ROX Mix and 40nM of primer mix (forward and reverse primers were pre-mixed; primers sequences are indicated in Table 3). Expression level of the house-keeping gene Glyceraldehyde 3-phosphate dehydrogenase (GAPDH) was used as reference. Each sample was run in technical triplicates, in case of high variability, one of the technical triplicates was removed. Number of biological replicates are indicated for each experiment (n).

Relative expression of the genes of interest were calculated by normalisation of the detected expression value to the geometric mean of the reference GAPDH gene using the ΔΔCt method[69]. More precisely, average cycle threshold (Avg Ct) was first calculated among technical triplicates or duplicates of each sample. Average delta Ct (Avg ΔCt) was then deduced by subtracting GAPDH Avg Ct to sample Avg Ct. The relative quantification (RQ) of cDNA for each gene was calculated as $2^{-\text{Avg}\Delta\text{Ct}}$. The fold change of each sample was calculated in reference to the average RQ of control samples group (control RQ) as: sample RQ/control RQ. The qPCR final results are shown as histograms, where each bar shows the average fold change of experimental replicates. Error bars are represented as standard error of the mean (SEM).

In utero electroporation surgery

For *in utero* electroporation (IUE), the *piggyBac* transposon system was used to avoid episomal plasmid loss upon cell division. pCAG-hyPBase and pPB-CAG-DsRed plasmids were kindly donated by Dr. Lucas Baltussen and have been previously described[70]. Plasmids was amplified with *E. Coli* culture, purified with EndoFree Plasmid Maxi kit and mixed together at a concentration of 1µg/µl per plasmid, with 0.05% of FastGreen in injectable water.

IUE was performed on E15.5 embryos. One before surgery, analgesia (Carprofen, dose 50mg/ml) was administered via drinking water to single caged pregnant females. On surgery day, pregnant females were anaesthetised using isoflurane and subcutaneous injection (10mg/kg of meloxicam and 0.1mg/kg of buprenorphine in injectable water). Females' eyes were kept moist using Viscotears eye gel. Anesthetised female was shaved on the abdomen, cleaned with chlorhexidine and moved to surgical area, where body temperature was monitored on a heating pad. Laparotomy and exteriorisation of the uterus were then performed. 10µl of DNA was loaded using micro loader tips into Ethylene Oxide (EtO) gas sterilised borosilicate glass capillaries (1.0 OD x 0.58 ID x 100L mm) which were pulled with a micropipette puller and the tip was broken using forceps. 1µl of solution containing the plasmid DNA was injected into the lateral ventricle of each embryos using a Femtojet pico dispenser, followed by electroporation (5 pulses 38V of 50ms with 1s interval) with EtO gas sterilised 5mm paddle type electrodes. The uterus was gently reinserted into the abdomen, then abdominal wall and skin were sutured separately. Mice were placed in a recovery chamber for a few hours. Analgesia (Carprofen, dose 50mg/ml) was administrated in drinking water for the following 48 hours. Electroporated embryos were harvested at P2.

Software for cell migration analysis

Distance.gui software was used to analyse PROX1+ cells distribution within the forming DG. It was written by Dr. Vivien Labat-gest and kindly donated by Prof. Federico Luzzati. The software calculates the distance in pixels between a point and line, which in this case are single PROX1+ cells and their migration line, respectively (schematic in Fig. 2.F). Therefore, the software input files for each image are the ImageJ cell counter result *.xml* file (representing PROX1+ cells points coordinates) and the XY coordinates of the reference line extracted from ImageJ as a *.txt* file

(representing the migration line). The output file is a *.txt* file containing a list of numbers representing the distance in pixel of each PROX1+ cell from the migration line. For each picture, the range of PROX1+ cell distribution (most distant cell from the migration line) was used to divide the forming DG area in 10 bins, then percentage of PROX1+ cell per bin was calculated and plotted as a line (Fig. 2.F and 5.I). Cells in bin #1-5 would be closer to the migration line, therefore representing the lower DG blade, compared to cells in bin #6-10, representing the upper DG blade.

Statistical and image analysis

H&E and *ISH* stained sections were acquired with Leica DM750 light microscope, and LAS (Leica Application Suite) EZ software was used for acquisition. Sections processed for EdU, TUNEL and immunofluorescence staining were imaged using Leica TCS SPE confocal microscope with 10x, 20x and 40x objectives. LAS AF software was used for acquisition. Acquisitions were performed as 1.5µm Z-stacks, with bidirectional X. For image analysis and counting, ImageJ and QuPath softwares were used. For cell quantification, 5 different images were acquired and counted per analysed area for each sample.

Statistical analysis of cell number quantification and qPCR analysis was performed on Prism 7 (Graphpad), calculating student's unpaired *t-tests*, when comparing two groups, or ordinary one-way ANOVA, when comparing three or more groups. Analyses were performed parametrically, upon confirmation of samples normal distribution. Histograms represent average quantification from the indicated number of biological replicates (n, minimum 3). Error bars for cell number quantification represent standard deviation (SD). Error bars for qPCR fold change analysis represent standard error of the mean (SEM). Data shown as percentage were processed with angular transformation before statistical analysis. P value is indicated as: ns:$p>0.05$; *:$p\leq0.05$; **:$p\leq0.01$; ***:$p\leq0.001$; ****:$p\leq0.0001$.

Antigen	Host	Dilution	Vendor	Catalog #	65°C	95°C
ALDH1L1	rabbit	1:500	Abcam	ab87117	e	
Caspase	rabbit	1:400	R&D system	AF835		
GFAP-Cy3	mouse	1:500	Sigma	C9205		
LEF1	rabbit	1:200	Cell Signalling	2230P		e
NF1A	rabbit	1:500	Active Motif	39397	e	
NF1B	rabbit	1:200	Abcam	ab185738	e	
PROX1	rabbit	1:500	BioLegend	PRB-238C	e, p	
REELIN	mouse	1:200	Abcam	ab78540	e	
SOX2	goat	1:500	Neuromics	GT15098	e	p
SOX9	goat	1:200	R&D system	AF3075	e	
TBR2	rabbit	1:500	Abcam	ab23345		e, p
YFP	rat	1:1000	Fine chemical products	04404-84		

Table 1: List of primary antibodies used. Antigen retrieval protocol (30 minutes in 65°C waterbath or 15 minutes in 95°C decloaking chamber) was performed for the indicated samples (e: embryos; p: pups).

Fluorophore	Host/reactivity species	Dilution	Vendor	Catalog #
Alexa 568	Donkey anti-Rabbit	1:500	Thermo Fisher Scientific	A10042
Alexa 647	Donkey anti-Rabbit	1:500	Thermo Fisher Scientific	A31573
Alexa 568	Donkey anti-Goat	1:500	Thermo Fisher Scientific	A11057
Alexa 647	Donkey anti-Goat	1:500	Thermo Fisher Scientific	A21447
Alexa 594	Donkey anti-Mouse	1:500	Thermo Fisher Scientific	A21203
Alexa 555	Donkey anti-Mouse	1:500	Thermo Fisher Scientific	A31570
Alexa 488	Donkey anti-Rat	1:500	Thermo Fisher Scientific	A21208
DAPI 300μM		1:500	Thermo Fisher Scientific	D1306

Table 2: List of secondary antibodies and nuclear staining used.

Target	Forward primer (5'- … -3')	Reverse primer (5'- … -3')	Supplier and Catalog #
Gapdh	TTCACCACCATGGAGAAGGC	CCCTTTTGGCTCCACCCT	Eurofins
Sox9	AAGAAAGACCACCCCGATTACA	CAGCGCCTTGAAGATAGCATT	Eurofins
Nf1a	CTTTGTACATGCAGCAGGAC	TTCCTGCAGCTATTGGTGTTT	Eurofins
Nf1b	GTGGAACCGGTGAATCTTTC	TCTGTCCTGGGCTCTATTCC	Eurofins
Aldh1l1	N/A	N/A	Qiagen PPM27706B-200
Cxcr4	N/A	N/A	Qiagen PPM03149E-200
Cxcl12	TGCATCAGTGACGGTAAACCA	TTCTTCAGCCGTGCAACAATC	Eurofins
Reln	TTACTCGCACCTTGCTGAAAT	CAGTTGCTGGTAGGAGTCAAAG	Eurofins
Vldlr	GGCAGCAGGCAATGCAATG	GGGCTCGTCACTCCAGTCT	Eurofins

Table 3: List of primers used for qPCR.

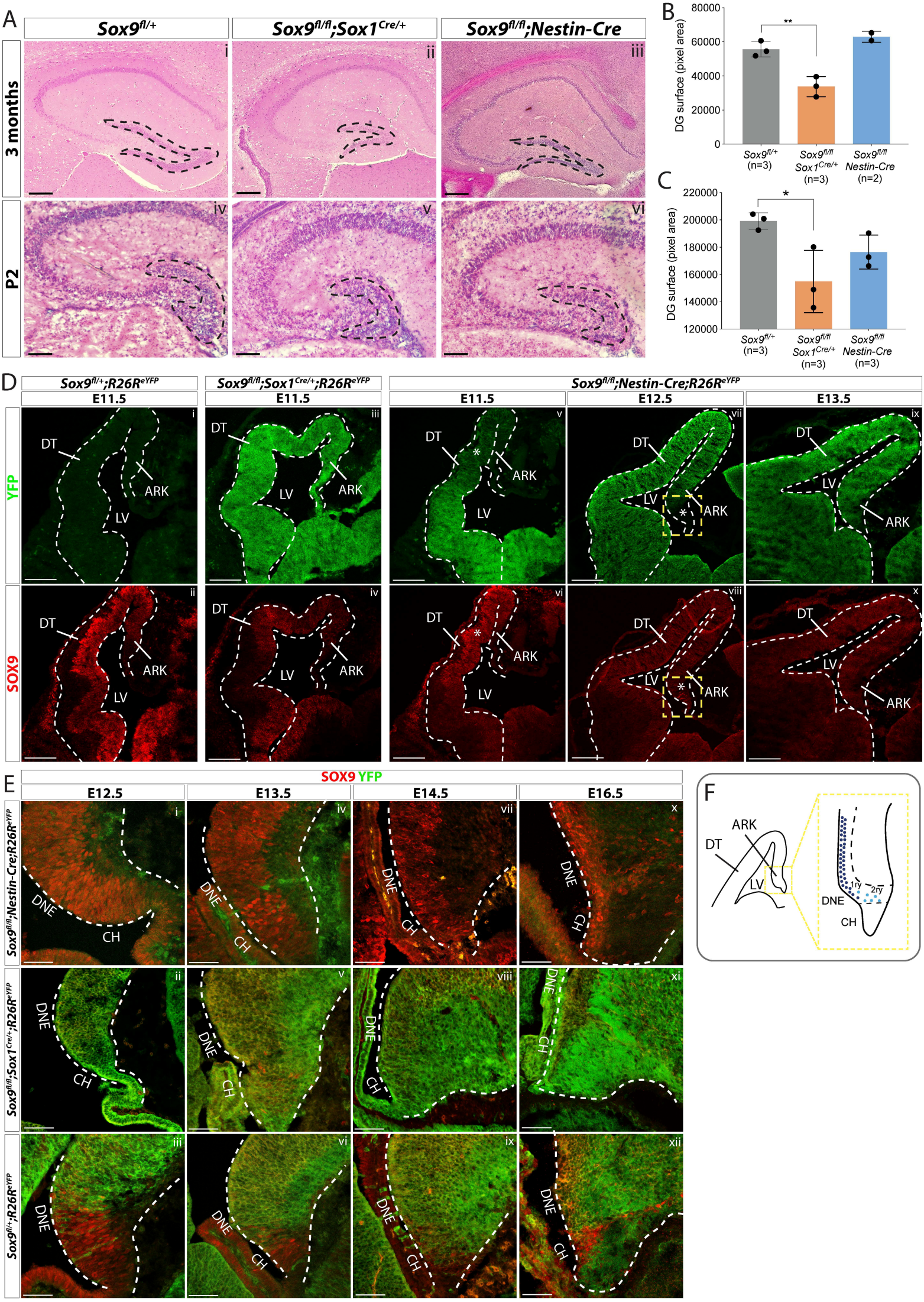
A
Sox9fl/+
Sox9fl/fl;Sox1Cre/+
Sox9fl/fl;Nestin-Cre
3 months
P2
i
ii
iii
iv
v
vi
B
DG surface (pixel area)
80000
60000
40000
20000
0
**
Sox9fl/+ (n=3)
Sox9fl/fl Sox1Cre/+ (n=3)
Sox9fl/fl Nestin-Cre (n=2)
C
DG surface (pixel area)
220000
200000
180000
160000
140000
120000
*
Sox9fl/+ (n=3)
Sox9fl/fl Sox1Cre/+ (n=3)
Sox9fl/fl Nestin-Cre (n=3)
D
Sox9fl/+;R26ReYFP
Sox9fl/fl;Sox1Cre/+;R26ReYFP
Sox9fl/fl;Nestin-Cre;R26ReYFP
E11.5
E11.5
E11.5
E12.5
E13.5
YFP
SOX9
DT
ARK
LV
E
SOX9 YFP
E12.5
E13.5
E14.5
E16.5
Sox9fl/fl;Nestin-Cre;R26ReYFP
Sox9fl/fl;Sox1Cre/+;R26ReYFP
Sox9fl/+;R26ReYFP
DNE
CH
F
ARK
DT
LV
1ry
2ry
DNE
CH

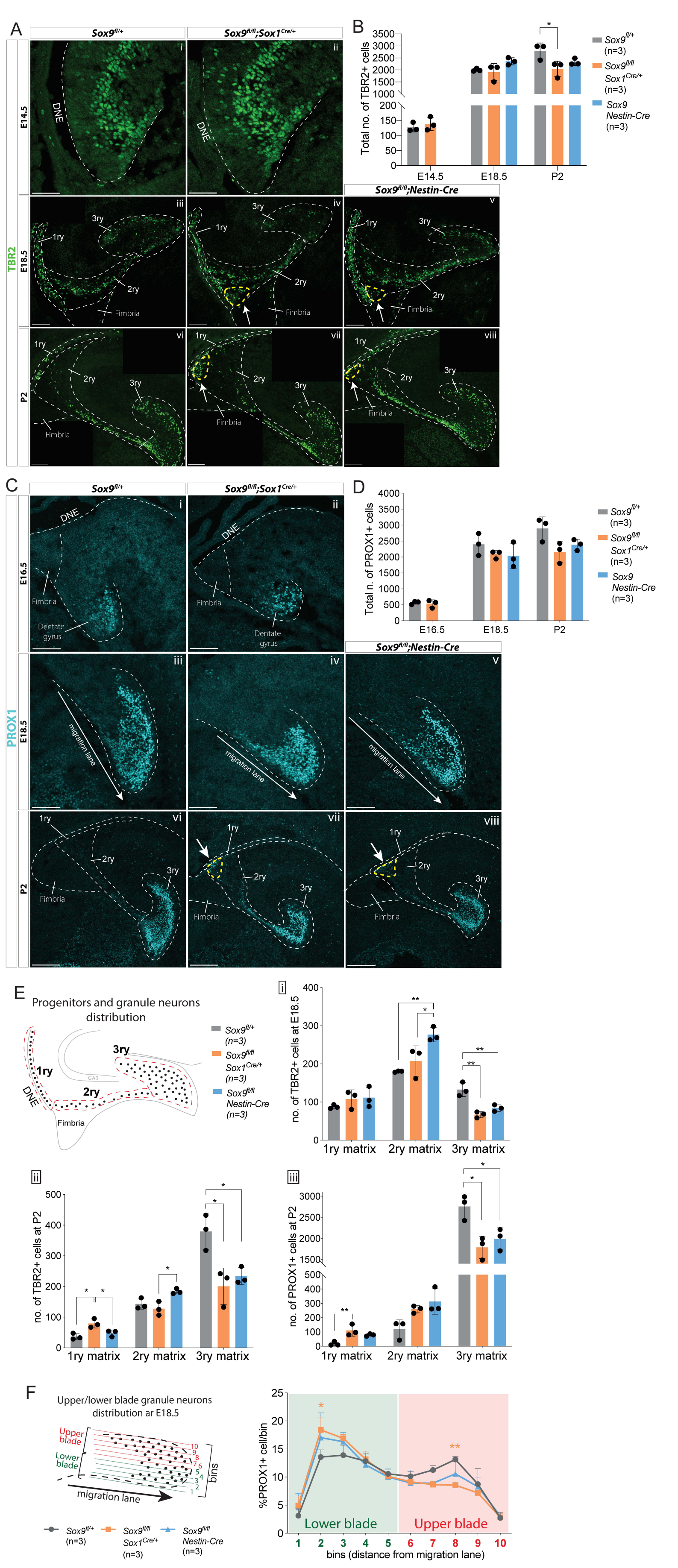
A
Sox9fl/+
Sox9fl/fl;Sox1Cre/+
Sox9fl/fl;Nestin-Cre
TBR2
E14.5
E18.5
P2
DNE
1ry
2ry
3ry
Fimbria
B
Total no. of TBR2+ cells
E14.5
E18.5
P2
Sox9fl/+ (n=3)
Sox9fl/fl Sox1Cre/+ (n=3)
Sox9 Nestin-Cre (n=3)
C
PROX1
E16.5
E18.5
P2
Dentate gyrus
migration lane
D
Total n. of PROX1+ cells
E
Progenitors and granule neurons distribution
CA3
no. of TBR2+ cells at E18.5
no. of TBR2+ cells at P2
no. of PROX1+ cells at P2
1ry matrix
2ry matrix
3ry matrix
F
Upper/lower blade granule neurons distribution ar E18.5
Upper blade
Lower blade
bins
%PROX1+ cell/bin
Lower blade
Upper blade
bins (distance from migration lane)

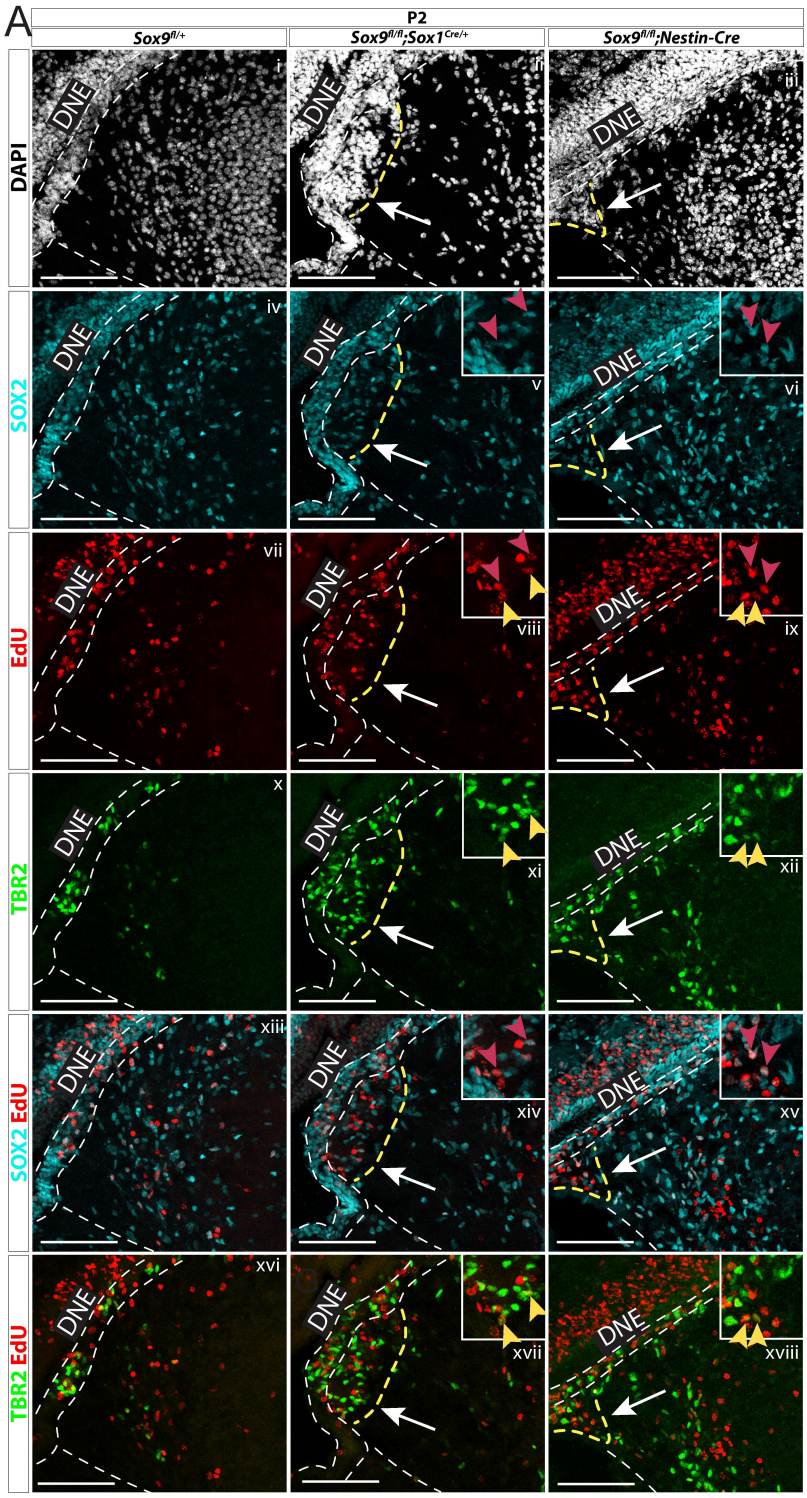
A
P2
Sox9fl/+
Sox9fl/fl;Sox1Cre/+
Sox9fl/fl;Nestin-Cre
DAPI
SOX2
EdU
TBR2
SOX2 EdU
TBR2 EdU
DNE

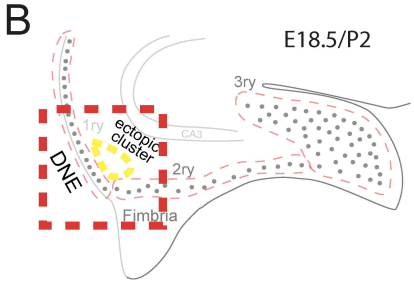
B
E18.5/P2
3ry
1ry
ectopic cluster
CA3
2ry
DNE
Fimbria

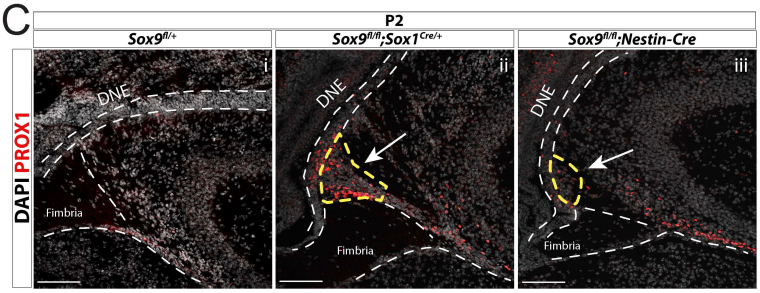
C
P2
Sox9fl/+
Sox9fl/fl;Sox1Cre/+
Sox9fl/fl;Nestin-Cre
DAPI PROX1
DNE
Fimbria

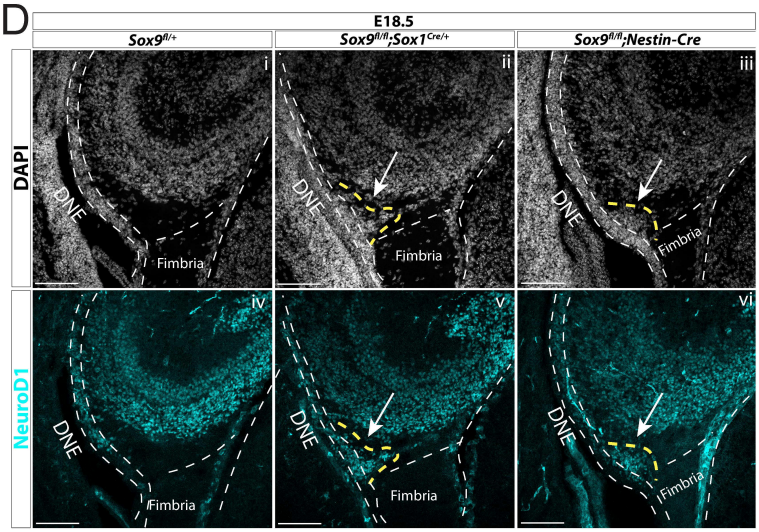
D
E18.5
Sox9fl/+
Sox9fl/fl;Sox1Cre/+
Sox9fl/fl;Nestin-Cre
DAPI
NeuroD1
DNE
Fimbria

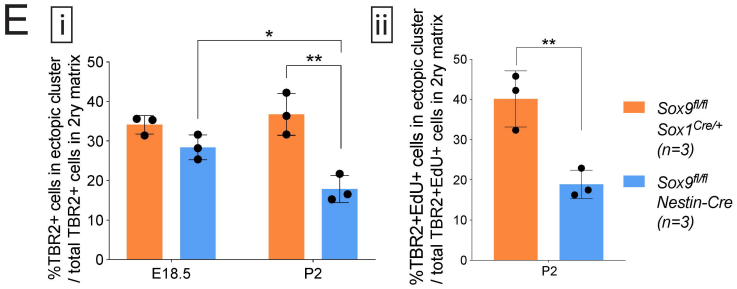
E
%TBR2+ cells in ectopic cluster / total TBR2+ cells in 2ry matrix
E18.5
P2
%TBR2+EdU+ cells in ectopic cluster / total TBR2+EdU+ cells in 2ry matrix
Sox9fl/fl Sox1Cre/+ (n=3)
Sox9fl/fl Nestin-Cre (n=3)

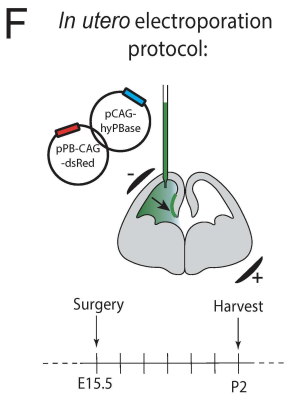
F
In utero electroporation protocol:
pCAG-hyPBase
pPB-CAG-dsRed
Surgery
Harvest
E15.5
P2

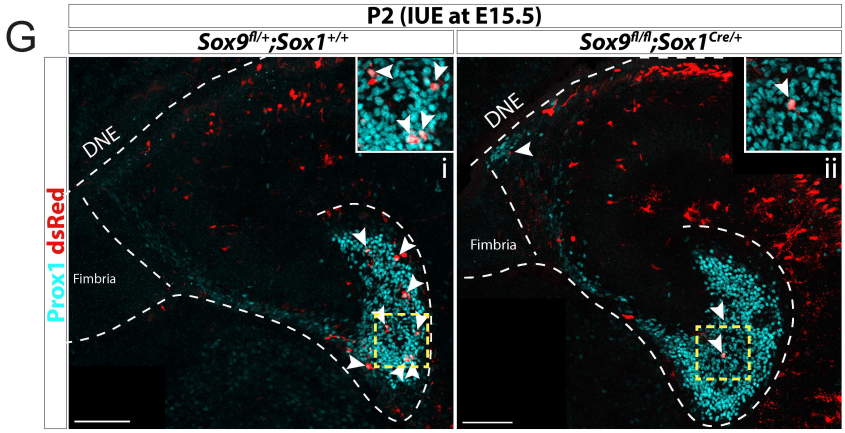
G
P2 (IUE at E15.5)
Sox9fl/+;Sox1+/+
Sox9fl/fl;Sox1Cre/+
Prox1 dsRed
DNE
Fimbria

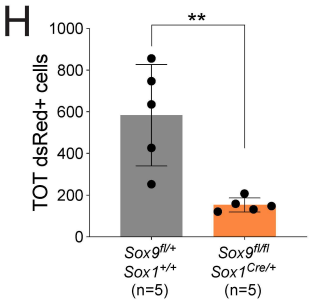
H
TOT dsRed+ cells
Sox9fl/+ Sox1+/+ (n=5)
Sox9fl/fl Sox1Cre/+ (n=5)

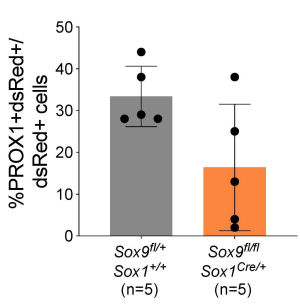
I
%PROX1+dsRed+/ dsRed+ cells
Sox9fl/+ Sox1+/+ (n=5)
Sox9fl/fl Sox1Cre/+ (n=5)

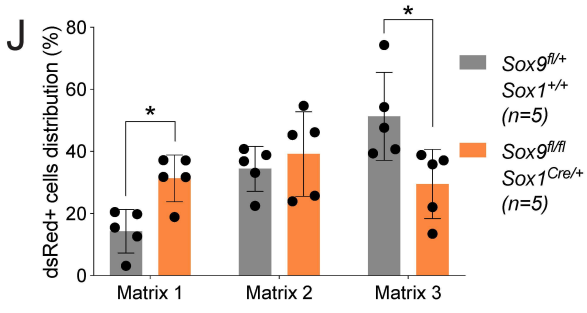
J
dsRed+ cells distribution (%)
Matrix 1
Matrix 2
Matrix 3
Sox9fl/+ Sox1+/+ (n=5)
Sox9fl/fl Sox1Cre/+ (n=5)

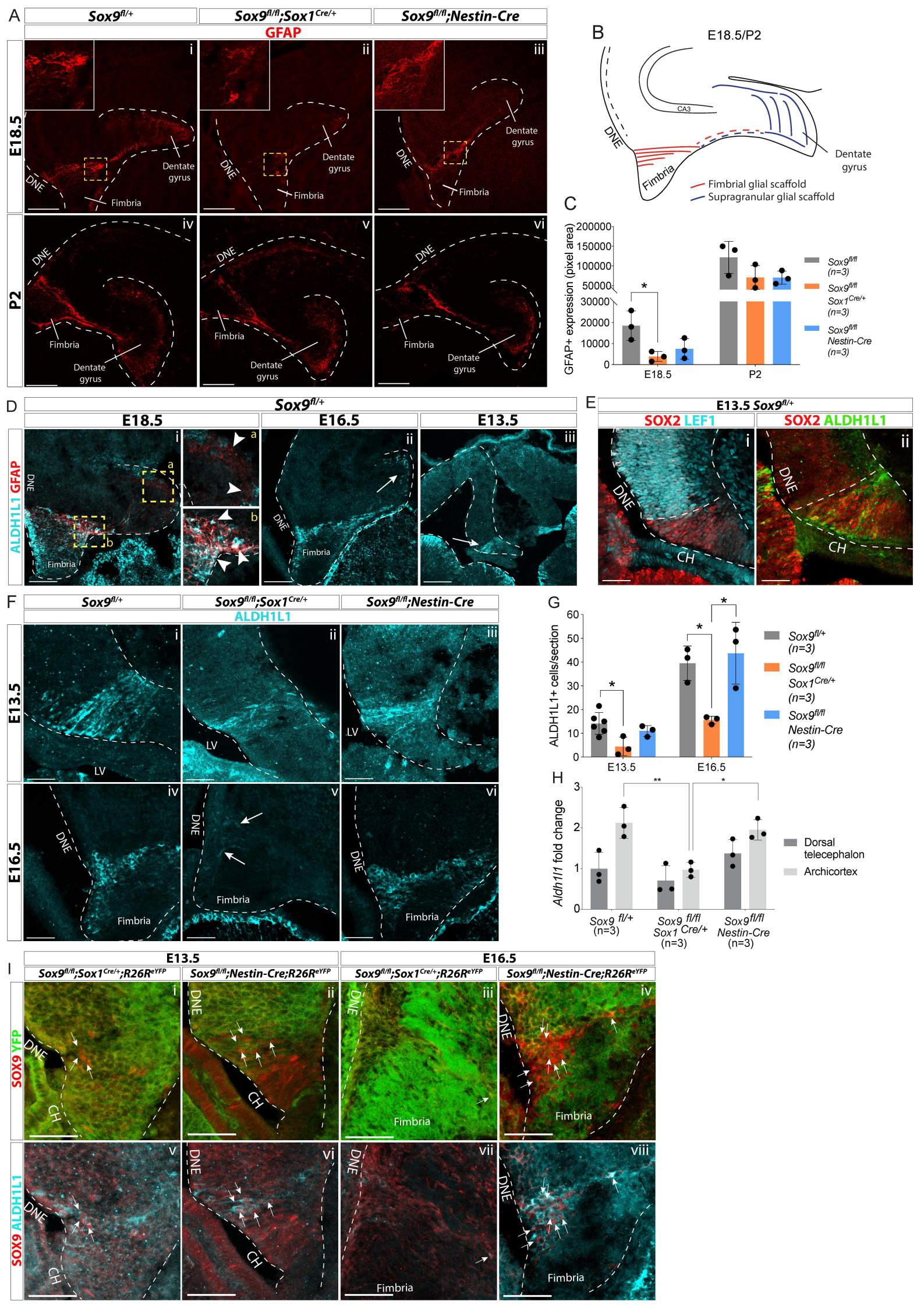
A
Sox9fl/+
Sox9fl/fl;Sox1Cre/+
Sox9fl/fl;Nestin-Cre
GFAP
E18.5
P2
DNE
Dentate gyrus
Fimbria
B
E18.5/P2
CA3
Fimbrial glial scaffold
Supragranular glial scaffold
C
GFAP+ expression (pixel area)
E18.5
P2
Sox9fl/fl (n=3)
Sox9fl/fl Sox1Cre/+ (n=3)
Sox9fl/fl Nestin-Cre (n=3)
D
Sox9fl/+
E18.5
E16.5
E13.5
ALDH1L1 GFAP
E
E13.5 Sox9fl/+
SOX2 LEF1
SOX2 ALDH1L1
CH
F
Sox9fl/+
Sox9fl/fl;Sox1Cre/+
Sox9fl/fl;Nestin-Cre
ALDH1L1
LV
G
ALDH1L1+ cells/section
H
Aldh1l1 fold change
Dorsal telecephalon
Archicortex
I
SOX9 YFP
SOX9 ALDH1L1

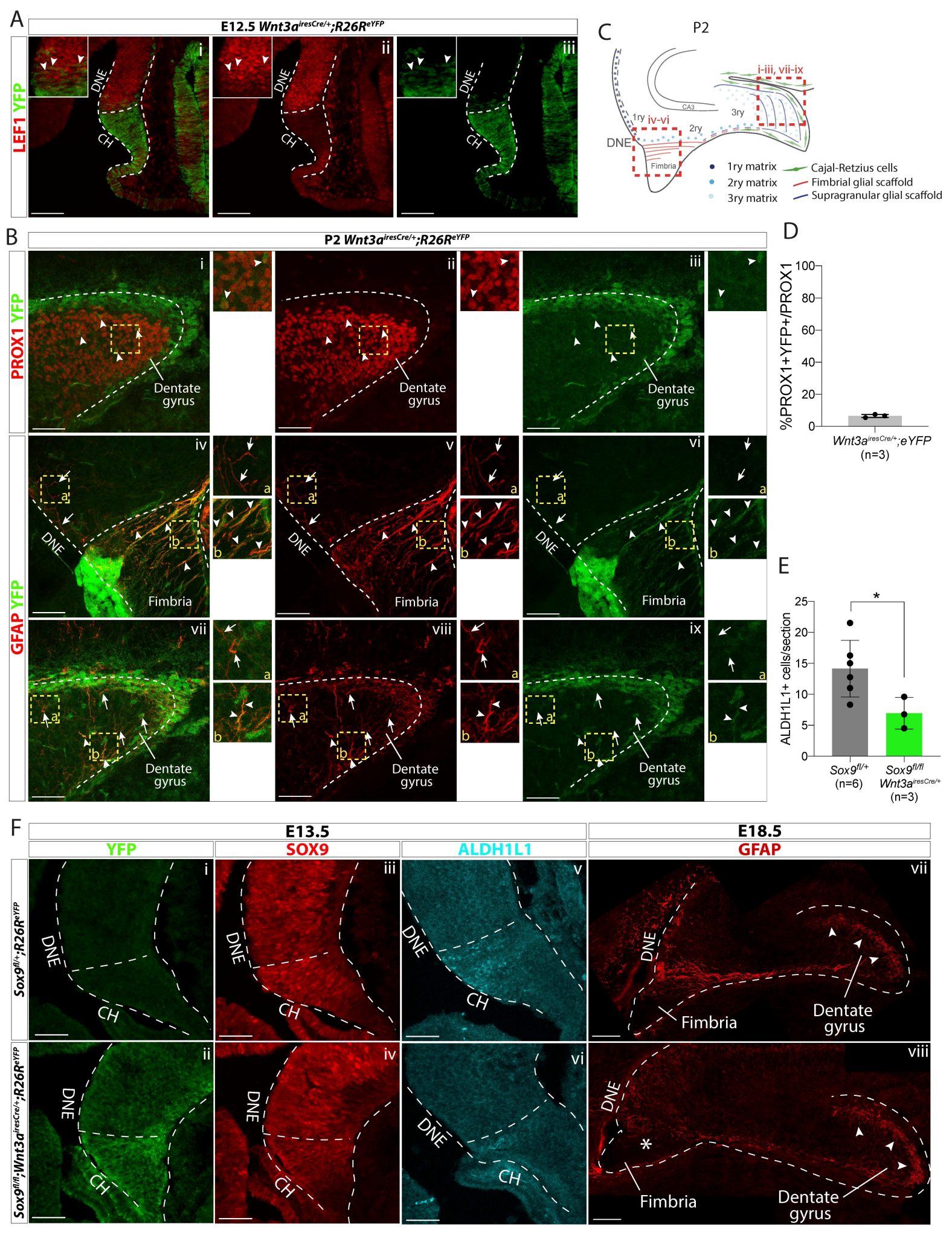
A
E12.5 Wnt3a iresCre/+;R26R eYFP
LEF1 YFP
i
ii
iii
DNE
CH
C
P2
i-iii, vii-ix
CA3
3ry
1ry
iv-vi
2ry
DNE
Fimbria
1ry matrix
2ry matrix
3ry matrix
Cajal-Retzius cells
Fimbrial glial scaffold
Supragranular glial scaffold
B
P2 Wnt3a iresCre/+;R26R eYFP
PROX1 YFP
GFAP YFP
Dentate gyrus
Fimbria
DNE
a
b
D
%PROX1+YFP+/PROX1
100
80
60
40
20
0
Wnt3a iresCre/+;eYFP
(n=3)
E
ALDH1L1+ cells/section
25
20
15
10
5
0
*
Sox9 fl/+
(n=6)
Sox9 fl/fl
Wnt3a iresCre/+
(n=3)
F
E13.5
E18.5
YFP
SOX9
ALDH1L1
GFAP
Sox9 fl/+;R26R eYFP
Sox9 fl/fl;Wnt3a iresCre/+;R26R eYFP
DNE
CH
Fimbria
Dentate gyrus
*

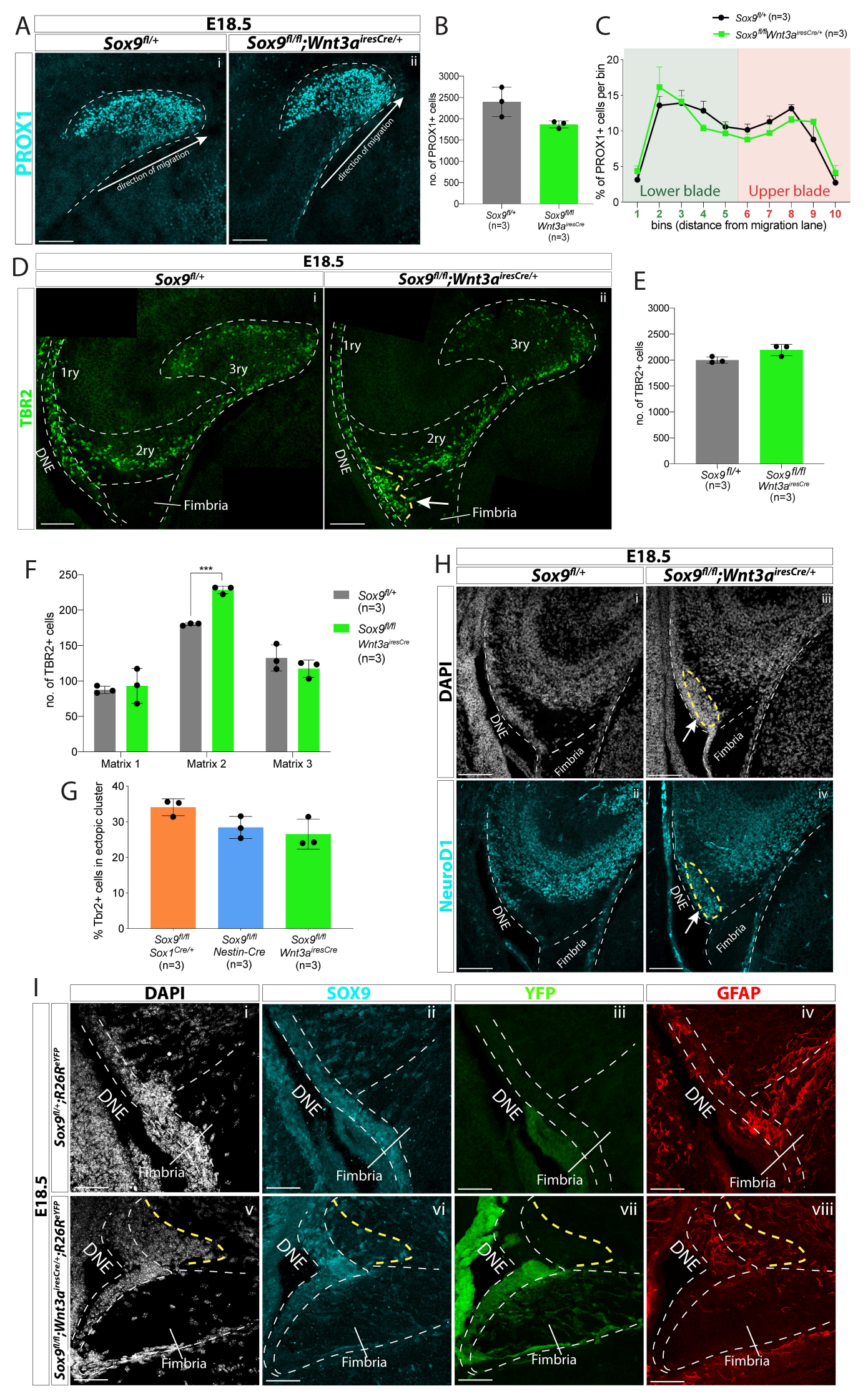
A
E18.5
Sox9fl/+
Sox9fl/fl;Wnt3airesCre/+
PROX1
i
ii
direction of migration
B
no. of PROX1+ cells
3000
2500
2000
1500
1000
500
0
Sox9fl/+ (n=3)
Sox9fl/fl Wnt3airesCre (n=3)
C
Sox9fl/+ (n=3)
Sox9fl/flWnt3airesCre/+ (n=3)
% of PROX1+ cells per bin
Lower blade
Upper blade
bins (distance from migration lane)
D
E18.5
Sox9fl/+
Sox9fl/fl;Wnt3airesCre/+
TBR2
1ry
2ry
3ry
DNE
Fimbria
E
no. of TBR2+ cells
Sox9fl/+ (n=3)
Sox9fl/fl Wnt3airesCre (n=3)
F
no. of TBR2+ cells
***
Matrix 1
Matrix 2
Matrix 3
Sox9fl/+ (n=3)
Sox9fl/fl Wnt3airesCre (n=3)
G
% Tbr2+ cells in ectopic cluster
Sox9fl/fl Sox1Cre/+ (n=3)
Sox9fl/fl Nestin-Cre (n=3)
Sox9fl/fl Wnt3airesCre (n=3)
H
E18.5
Sox9fl/+
Sox9fl/fl;Wnt3airesCre/+
DAPI
NeuroD1
iii
iv
I
DAPI
SOX9
YFP
GFAP
E18.5
Sox9fl/+;R26ReYFP
Sox9fl/fl;Wnt3airesCre/+;R26ReYFP
v
vi
vii
viii

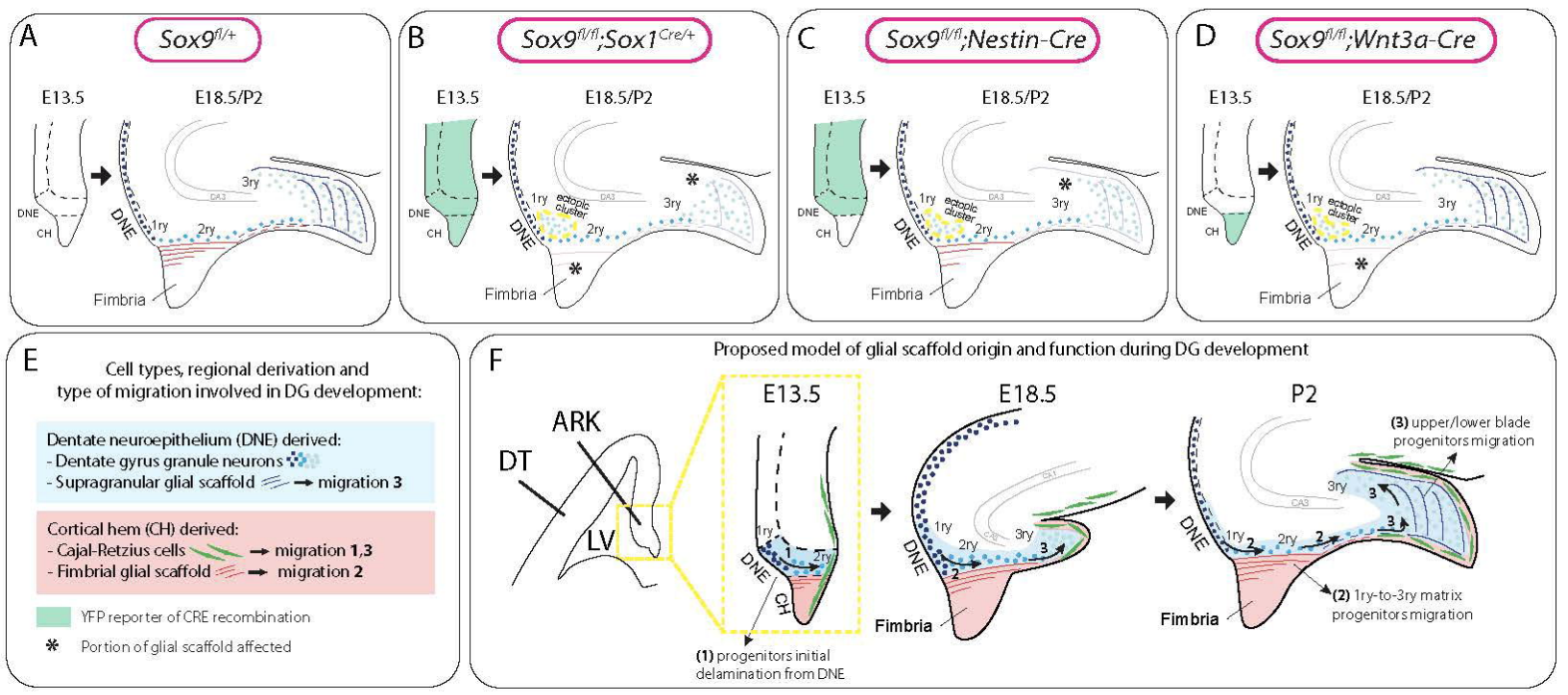
A
Sox9fl/+
B
Sox9fl/fl;Sox1Cre/+
C
Sox9fl/fl;Nestin-Cre
D
Sox9fl/fl;Wnt3a-Cre
E13.5
E18.5/P2
DNE
CH
1ry
2ry
3ry
ectopic cluster
Fimbria
E
Cell types, regional derivation and
type of migration involved in DG development:
Dentate neuroepithelium (DNE) derived:
- Dentate gyrus granule neurons
- Supragranular glial scaffold → migration 3
Cortical hem (CH) derived:
- Cajal-Retzius cells → migration 1,3
- Fimbrial glial scaffold → migration 2
YFP reporter of CRE recombination
Portion of glial scaffold affected
F
Proposed model of glial scaffold origin and function during DG development
ARK
DT
LV
E13.5
E18.5
P2
(1) progenitors initial delamination from DNE
(2) 1ry-to-3ry matrix progenitors migration
(3) upper/lower blade progenitors migration
Fimbria